Validation, Extensions, and Applications of the U^* Index Theory for Load Transfer Analysis of Vehicle Structures

by

Qingguo Wang

A thesis submitted to
The Faculty of Graduate Studies of
The University of Manitoba
in partial fulfillment of the requirements
of the degree of

Doctor of Philosophy

Department of Mechanical Engineering
University of Manitoba
Winnipeg

Abstract

A basic function of engineering structures is transferring the forces from the loading points to the supporting points. Understanding of the load transfer behavior is the foundation for engineering structural design. U^* index, which was introduced in 2005, is an indicator of load paths within structures. Load transfer analysis based on the U^* index has been developed as a new design paradigm for engineering structures. However, the U^* index theory has not been experimentally validated yet. Moreover, the U^* index theory is restricted to isotropic materials. Meanwhile, in the U^* index theory, the rotational DOFs are not considered. Consequently, it is imperative for the engineering community to validate and extend the U^* index theory.

In this thesis, firstly, an experimental study was performed to validate the U^* index theory. Secondly, a revised design of a vehicle component was accomplished based on the U^* index theory to demonstrate the effectiveness of the U^* related design criteria. Then, two new U^* indices (U^*_O and U^*_M) were proposed to eliminate the restrictions of the original U^* index. The proposed U^*_O index extended the application of the U^* index theory to orthotropic composite materials. The new U^*_M index was formulated by considering both translational and rotational DOFs, which makes the U^* index theory applicable for mechanical models under six DOFs. At the meantime, two applications were presented to show the capability of the newly proposed U^*_M index in automotive structural design. The applications demonstrate the load transfer analysis based on the newly proposed U^*_M index is an effective tool for designing desired automotive structures.

The thesis as a whole improved the U^* index theory to be more mature and capable for solving engineering problems with the higher complexities in both the material and the mechanical models. In addition to the structural analysis of ground vehicles, the extended U^* index theory has great potential to be applied in other kinds of engineering structures such as aircraft and ships.

Vita

Mr. Qingguo Wang was born on August 10th, 1984 in Shenyang City, Liaoning Province, China. He attended Dalian University of Technology in 2003 and obtained B. Eng. in Applied Mechanics in 2007. After that, he was enrolled by Dalian University of Technology with entrance examination waiver and he received M. Eng. in Applied Mechanics in 2010. Subsequently, he joined China First Automotive Works R&D Centre as a CAE engineer in charge of automotive structural static, fatigue, and vibration analyses. Mr. Wang started his Ph.D. program in University of Manitoba in 2013 and his research direction is advanced vehicle structural design through both computational and experimental methods.

Acknowledgement

First and foremost, I wish to express my heartfelt gratitude to my advisor, Dr. Christine Q. Wu for her help at the most difficult time of my life and for bringing me such an interesting research topic. Her support, patience, encouragement, and guidance helped me in all the time of the course of my research in the past three years.

Secondly, I would like to thank my co-advisor, Dr. Igor Telichev for his invaluable advice and help on my thesis, my project, and my paper publications, especially for his dedicated work in the final stages of the thesis.

My sincere appreciation goes to my advisory committee members, Dr. Raghavan Jayaraman, and Dr. Dagmar Svecova for their careful review, comments, and suggestions with regard to this thesis. My thanks also go to the thesis external examiner Dr. Jennifer Johrendt for her valuable review comments.

A special word of thanks is due to my lab fellows Dr. Khashayar Pejhan, Mr. Anton Kuznetcov, Mr. Wei Zhou, Mr. Hamid Giahi, and Dr. Yuming Sun. Their knowledge and suggestions are of great benefit to my research.

Finally, I would like to acknowledge my deepest gratitude to my parents and my wife for their numerous sacrifices made on my behalf, without that I could not have achieved my goals.

I dedicate this to my beloved wife Shuo Du.

Table of Contents

List of Tables

List of Figures

Nomenclature

U	Total strain energy of the system
U'	Total strain energy of the modified system
P_A	Applied load to the system
P_A'	Applied load to the modified system
d_i	Displacement at the point i
K_{ij}	Internal stiffness between points i and j
U^*	Original load transfer index
U_O^*	Load transfer index for orthotropic materials
U_M^*	Load transfer index for six DOFs systems
$g^{(-)}$	Stiffness decay vector
U_1^*	Load transfer index for the applied loads
U_2^*	Load transfer index for the reaction forces
U_{sum}^*	Summation of U^*_1 and U^*_2

Chapter 1

Introduction

1.1 Motivation

The automotive industry was led into a new era by the development of electrical and unmanned vehicles. However, one thing which has never changed for automotive designers is the pursuit of the advanced vehicle structures in terms of safety and weight-efficiency. Safety occupies the most significant place in vehicle design because it is directly related to human life. 32,166 persons were dead during the vehicle accidents happened in 2015 according to Fatality Analysis Report System of National Highway Traffic Safety Administration. Recently, the environmental issues have been increasingly focused by many countries and areas of the world. According to (Scientists 2014), 30 percent of all U.S. emissions are produced by automobiles. Increasing weight-efficiency is one of the best ways to lower the energy consumption of vehicles (Casadei and Broda 2008). The highly weight-efficient vehicle can help manufacturers to not only reduce the cost of production but also satisfy the increasingly demand of environmental protection.

A key function of the vehicle structure is to provide required strength and stiffness to bear internal and external loads during driving and accidents. An ideal vehicle structure can

reach the demanded strength and stiffness by using the minimum material. Consequently, the primary task before achieving such an ideal structure is to have a thorough understanding of the structural behavior from the viewpoint of load transmission which is regarded as load transfer (or load paths) analysis (Gharibi et al. 2017; Harasaki and Arora 2001a; Kelly et al. 2001; Takahashi and Sakurai 2005). A good knowledge of the load transfer behavior can help designers to ensure that the structure has the intended function, reliable mechanical performance, and desired weight-efficiency (Tamijani and Gharibi 2016).

Load transfer analysis is the foundation of designing load bearing structures and it is a popular research topic in both civil and mechanical engineering (Kelly et al. 2011; Palmisano and Elia 2014). It was massively applied in designing air and ground vehicles where the structural strength and the weight-efficiency are both essential (Tamijani and Gharibi 2016; Wang et al. 2010). It is difficult to track the load paths in a structure because the transmission of the applied forces is invisible. It had been a long dream for design engineers to achieve such load paths as presented in Figure 1.1.

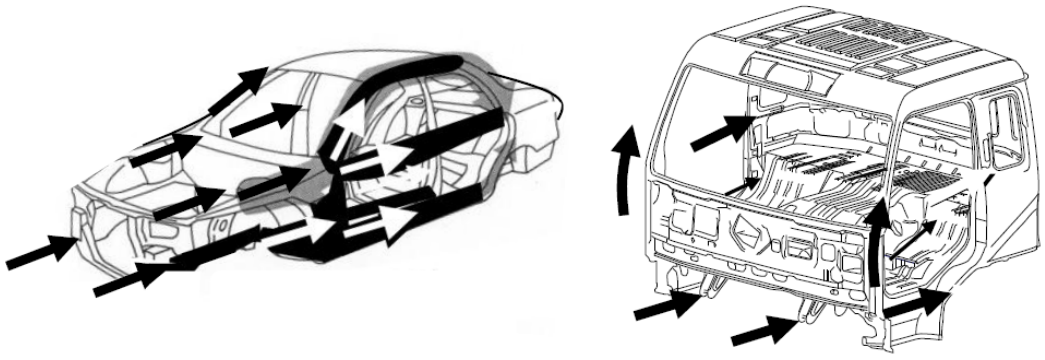

Figure 1.1: Examples of load paths in vehicle structures (Wang et al. 2010).

U^*, the load transfer index, was firstly introduced by Takahashi in 2005 (Takahashi and Sakurai 2005). It is one of the methods proposed for solving this practical engineering problem (load path calculation) in the past two decades (Marhadi and Venkataraman 2009). The U^* index characterizes the load paths based on the structural stiffness and thus prevent the misleading by stress concentration problems in load path analysis. In addition, the U^* index can be applied as design criteria for designing lightweight and high stiffness structures (Koboyashi et al. 2011). However, the U^* index theory assumes the materials as linear elastic and isotropic. Moreover, the rotational degrees of freedom (DOFs) have to be neglected during the computation of the U^* index. These assumptions considerably restrain the application of the U^* index theory in solving real life engineering problems. Accordingly, the motivation of the thesis is to develop the U^* index theory into a more universal form by eliminating its theoretical limitations and extend the application of the U^* index theory to structural analysis with higher complexities in both material and mechanical models.

1.2 Literature review

1.2.1 Methods of load transfer analysis

Load paths are a concept for tracking the transferred forces within the structure starting from the loading points and ending at the supporting points. Unlike stresses and displacements, the load path is hard to obtain based on the fundamental mathematics and mechanics (Harasaki and Arora 2001a). Benefitting from the development of finite element analysis (FEA), multiple methods were proposed for visualizing load paths of structures.

Stress trajectory method was one of the methods where stress flows were used to calculate load paths of structures (Gharibi et al. 2017; Kelly et al. 2011; Kelly et al. 2001; Tamijani and Gharibi 2016). However, three drawbacks make this method inadequate for load transfer analysis of vehicle structures. The first one is that the information of stresses is not sufficient to reflect the load transfer of a full structure because stresses only represent a local loading state (Harasaki and Arora 2001a). Secondly, stress concentration problems caused by geometrical irregularities like a hole or a notch render the method misleading (Harasaki and Arora 2001a; Pejhan et al. 2015a; Wang et al. 2010; Wang et al. 2015). Thirdly, the information obtained from the stress trajectory method is similar to a conventional finite element analysis (Pejhan et al. 2015c). Harasaki introduced a concept of "transferred forces" (Harasaki and Arora 2001a) to demonstrate the load paths in structures without being affected by issues of stress concentration. Design optimizations were conducted based on the transferred forces (Harasaki and Arora 2002; Harasaki and Arora 2001b), where formal optimization techniques such as sensitivity analyses or optimization algorithms are not needed. However, in this method, removing the interest element from the finite element model may induce an unstable mechanical system (Wang et al. 2017a).

An alternative method for computing the load paths is the load transfer index (U^*), which was firstly introduced by Takahashi et al. (Takahashi and Sakurai 2005). The U^* index represents the internal stiffness between the loading point and an arbitrary point of the structure. The U^* index theory suggests that the parts with the highest U^* values transfer the main portion of the loads. This method identifies the load paths based on the stiffness of the structure, thus it is not sensitive to the stress concentrations. At the same time, the method does not need any elimination of elements from the finite element model during the

calculation. Furthermore, rather than calculating the load path, the U^* analysis can provide designers with the insights of the structural issues, therefore leading to better structural design (Wang et al. 2017b; Wang et al. 2017c).

1.2.2 Development of the U* index theory

The U^* index theory was initially formulated for linear elastic and isotropic materials under a static force with single loading point (Takahashi and Sakurai 2005). After that, researchers concentrated on the development of the theory. Sakurai et al. proposed the mathematical expression of the U^* index for multiple loading points (Sakurai et al. 2007a). Inspection loads methods was introduced to improve the computational efficiency of the U^* analysis (Sakurai et al. 2007b). Wang et al. introduced U^{**} index as a complimentary concept of the U^* index for structures under distributed loads (Wang et al. 2010). Takahashi et al. modified the U^* index theory to be valid for dynamic loads (Takahashi et al. 2013). Pejhan et al. extended the U^* index theory into nonlinear elastic materials (Pejhan et al. 2015b; Wang et al. 2017a). A new concept of U^*_{sum} index was introduced by Naito et al. to evaluate the structural weight-efficiency and the similarity of load path dispersion (Koboyashi et al. 2011; Naito et al. 2011).

The automotive industry has been greatly benefitted from the U^* index theory. The load transfer analysis based on the U^* index has been used as a design criterion for vehicle structural analysis and design by automotive manufacturers such as Honda and Nissan (Hoshino et al. 2003; Koboyashi et al. 2011; Naito et al. 2012; Naito et al. 2011; Wang et al. 2010). For example, the U^* index theory was utilized to determine the appropriate locations for adding stiffeners to a car body (Akima et al. 2015). The maximum

deformation of the stiffened car body was decreased by more than 30% under side impact loading. It was also applied to locating the spot welds between sheet structures to achieve the maximum structural stiffness (Naito et al. 2012). Pejhan et al. applied the U^* index theory to lower the hot spot stress of the welds between window pillars in a bus structure (Pejhan et al. 2017a).

1.3 Objectives

Load transfer analysis based on the U^* index theory has been developed as a new design paradigm of vehicle structures. However, the U^* index theory is not mature enough. In other words, there is still room for improving the U^* index theory. The U^* index theory predicts load paths by the use of the concept of internal stiffness. Internal stiffness is the coupling stiffness between any two points in the structure. Takahashi et al. claimed that the load paths computed by the U^* index satisfy expectations from the engineering point of view (Wang et al. 2010), however those load paths have not been proven by any physical testing. In other words, validation of the U^* index theory through physical experiments is still lacking. Hence, the first objective of the thesis is to experimentally validate the U^* index theory.

The U^* index identifies the load transmission by evaluating the structural stiffness. Based on that, three design criteria (Uniformity, Continuity, and Consistency) were proposed for pursuing ideal stiffness distribution of structures. Sakurai et al. performed a design optimization of a cab structure based on those design criteria (Sakurai et al. 2003). In the mentioned literature, the U^* distributions of the structure are better in terms of the U^*

based design criteria, whereas the structural improvement from the viewpoints of mechanical performance and weight-efficiency cannot be seen. Naito et al. introduced the U^*_{sum} index as another design criterion for analysing the structural weight-efficiency (Naito et al. 2011). However, the effectiveness of the U^*_{sum} index in structural design improvement is also unknown. Therefore, the second objective of the thesis is to show the effectiveness of the U^* based design criteria on vehicle structural design. More specifically, the thesis demonstrates the structural modifications obtained by using the U^* based design criteria can indeed lead to the improvement of structural mechanical performance and weight-efficiency.

The original U^* index was arisen by assuming the structural material as linear elastic and isotropic but neglected the rotational degrees of freedom (DOFs) from the mechanical model of the structure (Naito et al. 2011; Takahashi and Sakurai 2005). Thus, the original U^* index cannot be applied in composite materials which are anisotropic instead of isotropic (Jones 1998). However, the composite materials are increasingly used in ground vehicles, ships, and aircrafts due to their extremely high stiffness to mass and strength to mass ratios (El-Abbasi and Meguid 2006; Jones 1998; Li et al. 2006; Pegoretti et al. 2002; Tarlochan and Ramesh 2012; Zhang and Yang 2009). For example, to achieve equal strength, composite parts can be 30-40% lighter than steel parts (Zhang et al. 2012). Moreover, the weight-efficiency of the composite structure can be further increased by appropriate reinforcements along the main load paths (Li et al. 2006; Zhang et al. 2012). Another issue caused by the assumptions of the original U^* index theory is that the original U^* index is invalid when the rotational DOFs are not negligible in the mechanical model of the structure. For instance, when plate and shell theories were applied for establishing the

mechanical model of a thin-walled structure subjected to the out-of-plane bending, the rotational DOFs could not be ignored (Niordson 2012). In this situation, the original U^* index is incapable for load path analysis. Here, a coupling issue is that the original U^* index is not compatible with shell elements which are governed by plate and shell theories (ANSYS 2013; Niordson 2012). However, plate and shell theories are essential for engineering computations of thin-walled structures (Dornisch et al. 2016; El-Abbasi and Meguid 2006; Kobelev 2016; Serra 2010). Moreover, engineers enjoy the advantages of shell elements over solid elements in computational efficiency and accuracy (Park et al. 2006; Simkins and Li 2003). Consequently, it is imperative to expand the application of the U^* index theory into composite materials and thin-walled structures, which is set as the third objectives of the thesis.

The whole thesis focuses on making the U^* index theory more capable for designing better vehicle structures with higher stiffness and lighter weight. Hence, the last objective of the thesis is to show the effectiveness of the extended U^* index theory in load transfer analysis through applications on vehicle structures and components.

1.4 Organization of the thesis

The remainder of the thesis is divided into seven chapters. A description of each is outlined below:

Chapter 2 reviews the original U^* index theory including the formulation of the U^* index, the visualization of the load paths, three design criteria based on the U^* index and the concept of the U^*_{sum} index.

Chapter 3 is devoted to the experimental validation of the U^* index theory. The load path of the sample structure, which is obtained from a static force testing is exactly the same as the load path calculated by the U^* index.

Chapter 4 demonstrates the effectiveness of the design criteria based on the U^* index through a design modification of a vehicle component. The work shows that the implementation of the U^* based design criteria can effectively lead to improvement of the structural performance and efficiency.

Chapter 5 proposes two new indices (U^*_O and U^*_M) for load transfer analysis of structures with higher complexities in material properties and mathematical models. To be more specific, firstly, the U^*_O index is introduced to extend the U^* index theory into orthotropic composite materials. Two case studies are performed on both unidirectional and woven fiber composites using the proposed U^*_O index. Then, the U^*_M index is established by considering both translational and rotational DOFs (i.e. six DOFs) in the mechanical model of the structure. The accuracy of the proposed U^*_M index is compared with the original U^* index.

Chapter 6 presents an application of the new U^*_M index in design analysis and modification of a complex thin-walled structure. The thin-walled structure is modeled by shell elements and therefore the proposed U^*_M index is applied for the load transfer analysis instead of the original U^* index. The application reveals the U^*_M index is an effective tool

for load transfer analysis of thin-walled structures. The design modification based on the U^*_M analysis increases the stiffness to mass ratio of the sample structure by 18.3%.

Chapter 7 gives another application of the U^*_M index to the load transfer analysis of a bus bay section for bus rollover protection. A static loading condition is designed as the equivalence force of the rollover impact based on the European regulation ECE R66. A thorough investigation of the load transmission of the bus bay section is presented. Multiple structural issues are found from the load transfer analysis. Recommendations are made for improving the bus structural performance during the rollover test.

Chapter 8 includes the conclusive remarks and the recommended future work in light of the whole thesis.

Chapter 2

Theoretical Preliminaries

2.1 Original U* index

The U^* index was first introduced by a Japanese research team led by Takahashi (Takahashi and Sakurai 2005). The U^* index represents the internal stiffness between the loading point and an arbitrary point in the structure. The internal stiffness is the coupling stiffness between any two points of the structure (Naito et al. 2011). Figure 2.1a shows a linear elastic body with loading point *A*, supporting point *B*, and an arbitrary point *C*. The springs are used to indicate the internal stiffness between any two points of the system.

In the system, the relations among force, displacement, and internal stiffness can be expressed as:

$$\begin{bmatrix} \boldsymbol{P_A} \\ \boldsymbol{P_B} \\ \boldsymbol{P_C} \end{bmatrix} = \begin{bmatrix} \boldsymbol{K_{AA}} & \boldsymbol{K_{AB}} & \boldsymbol{K_{AC}} \\ \boldsymbol{K_{BA}} & \boldsymbol{K_{BB}} & \boldsymbol{K_{BC}} \\ \boldsymbol{K_{CA}} & \boldsymbol{K_{CB}} & \boldsymbol{K_{CC}} \end{bmatrix} \begin{bmatrix} \boldsymbol{d_A} \\ \boldsymbol{d_B} \\ \boldsymbol{d_C} \end{bmatrix} \tag{2.1}$$

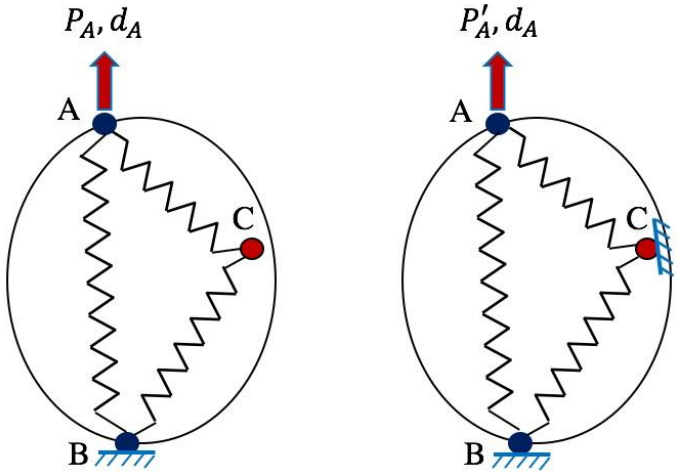

(a) (b)

Figure 2.1: Mechanical model of U^* calculation- a): Original system; b): Modified system.

In Equation 2.1, $\boldsymbol{K_{ij\ (i=A,B,C;j=A,B,C)}}$ is the internal stiffness tensor, $\boldsymbol{P_{i\ (i=A,B,C)}}$ and $\boldsymbol{d_{i\ (i=A,B,C)}}$ represent the force and the displacement vectors at the corresponding points respectively and both of them have three translational DOFs (Takahashi 1986). The resultant total strain energy of the original system (see Figure 2.1a) due to the external force is:

$$U = \frac{1}{2}\,\boldsymbol{P_A} \cdot \boldsymbol{d_A} \tag{2.2}$$

Since point *B* is fixed ($\boldsymbol{d_B} = 0$),

$$\boldsymbol{P_A} = \boldsymbol{K_{AA}}\boldsymbol{d_A} + \boldsymbol{K_{AC}}\boldsymbol{d_C} \tag{2.3}$$

After the substitution of $\boldsymbol{P_A}$ in Equation 2.2,

$$U = \frac{1}{2}\,\boldsymbol{P_A} \cdot \boldsymbol{d_A} = \frac{1}{2}(\boldsymbol{K_{AA}}\boldsymbol{d_A} + \boldsymbol{K_{AC}}\boldsymbol{d_C}) \cdot \boldsymbol{d_A} \tag{2.4}$$

By fixing point *C* ($\boldsymbol{d_C} = 0$) and forcing the same displacement ($\boldsymbol{d_A}$) at the point *A* as shown in Figure 2.1b, the total strain energy of the modified system is:

$$U' = \frac{1}{2}\,\boldsymbol{P'_A} \cdot \boldsymbol{d_A} = \frac{1}{2}\,(\boldsymbol{K_{AA}}\boldsymbol{d_A}) \cdot \boldsymbol{d_A} \tag{2.5}$$

where $\boldsymbol{P'_A}$ is the force at the point *A* of the modified system. Then, the original U^* index is defined as:

$$U^* = 1 - \frac{U}{U'} \tag{2.6}$$

Equation 2.6 can be rewritten as:

$$U^* = 1 - \frac{U}{U'} = [-\frac{U'}{U - U'}]^{-1} \tag{2.7}$$

By subtracting 1 and then adding 1 inside of the bracket, Equation 2.7 equals to:

$$[-\frac{U'}{U - U'} - \frac{U - U'}{U - U'} + 1]^{-1} = [1 - \frac{U}{U - U'}]^{-1} \tag{2.8}$$

Through the substitution of Equation 2.4 and 2.5, the Equation 2.8 can be written as:

$$U^* = \left[1 - \frac{2U}{(\boldsymbol{K_{AC}}\boldsymbol{d_C}) \cdot \boldsymbol{d_A}}\right]^{-1} \tag{2.9}$$

Equation 2.9 shows that the U^* index only varies with $\boldsymbol{K_{AC}}$ instead of $\boldsymbol{K_{AA}}$ and $\boldsymbol{K_{AB}}$. As a result, the U^* can characterize the internal stiffness between the loading point and an arbitrary point of the structure and thus identify the load paths of the structure.

In a structure, the applied force is mainly transferred through the locations having the strongest coupling stiffness with the loading point. Therefore, the line with the highest U^* values which is the ridge line of the U^* distribution is the main load path. If a vector $\boldsymbol{g}^{(-)}$ is defined as:

$$\boldsymbol{g}^{(-)} = -gradU^* \tag{2.10}$$

the main load path is the line with the smallest $\boldsymbol{g}^{(-)}$. The vector $\boldsymbol{g}^{(-)}$ is regarded as the "stiffness decay vector" (Wang et al. 2010).

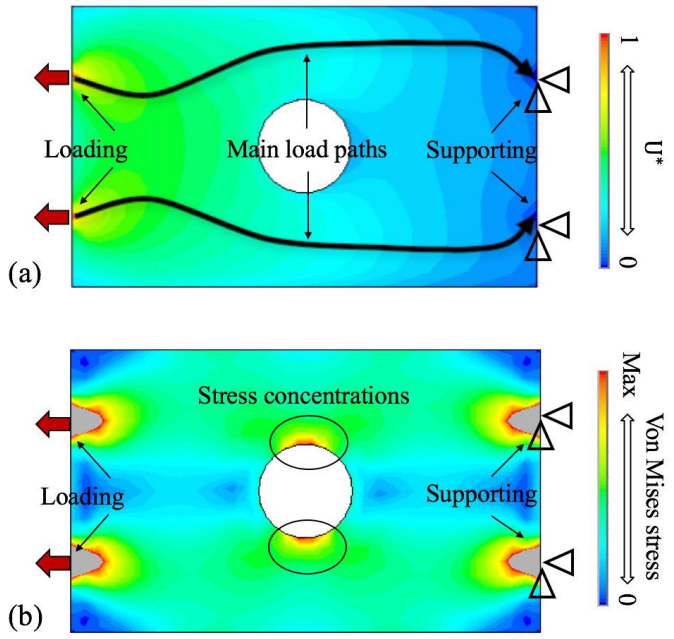

Figure 2.2: Load transfer analysis of a plate with a hole- a): U* distribution and main load paths; b): Von Mises stress distribution.

Figure 2.2a and Figure 2.2b elaborate U^* and stress distributions of a plate with a hole, respectively. The solid black lines shown in Figure 2.2a are the main load paths predicted by the U^* index, which satisfy the expectation form the engineering point of view (Wang et al. 2010). As can be seen in Figure 2.2b the higher stresses are formed in the vicinity of the hole. However, the hole is not important in transferring the forces, thus it is unreasonable to conclude the main load paths pass the locations with those higher stresses. The stress concentrations cause the load transfer analysis difficult (Naito et al. 2011).

2.2 Three U* driven design criteria

Uniformity, Continuity, and Consistency are three design criteria derived from the U^* index theory (Sakurai et al. 2003). Normally, the U^* index decreases from the maximum value of one (1) at the loading point to the minimum value of zero (0) at the supporting point. In Figure 2.3a, the solid line elaborates the variation of the U^* index along a path of a load bearing structure and the dash line depicts the U^* variation of the desirable condition. A uniform decay of the U^* index means the structural stiffness distribution is perfect, whereas in reality, the U^* variation is non-uniform because of the structural issues. An increase or decrease of the rate of the U^* decay indicates the stiffness in the corresponding part is higher or lower than other parts. The uniformity of the U^* decay is defined as the criterion to evaluate the rationality of the stiffness distribution of the structure. Structural modifications are required when the U^* curve is not uniform such as the solid line in Figure 2.3a. The effective structural modifications shall reduce the shade area shown in Figure 2.3a.

Figure 2.3b shows the "Continuity" of the U^* values along a path of a load bearing structure. If the U^* variation is uniform as depicted by the dash line in Figure 2.3a, the curvature of the entire U^* curve shall be constant. Otherwise, the curvature will suddenly increase or decrease as shown as the solid line in Figure 2.3b. Compared to the uniformity, the continuity of the U^* index reflects the rationality of the stiffness distribution of the structure from a different point of view.

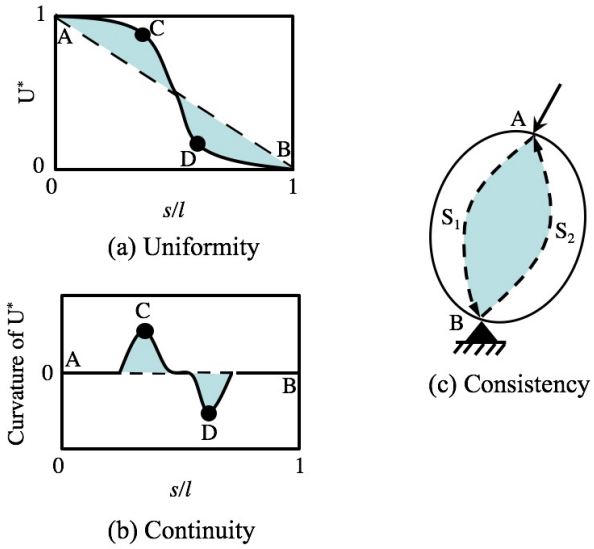

Figure 2.3: Illustration of the U* based design criteria- a): Uniformity; b): Continuity; c): Consistency.

It can be seen from Figure 2.3c that S_1 (from point *A*) and S_2 (from point *B*) represent the load paths of the applied force and the reaction force, respectively. In an ideal structure, the load path from the loading point should be consistent with the load path from the supporting point, which is known as the design criterion "Consistency". A structure with the consistent load paths can efficiently transfer the applied forces. When a structure is designed inappropriately, those load paths will be deviating from each other as illustrated in Figure 2.3c. The structural modification should aim at minimizing the deviation between the load paths S_1 and S_2.

2.3 U^*_{sum} index

The U^*_{sum} index was introduced to evaluate the weight-efficiency of load bearing structures in (Naito et al. 2011). As shown in Figure 2.4a, the U^* index presented above is considered as U^*_1 when point *A* is the loading point and point *B* is the supporting point. By switching the loading point with the supporting point of the structure, the U^*_2 index can be obtained as illustrated in Figure 2.4b. The U^*_2 index characterizes the load transfer of the reaction force from the supporting point *B* to the loading point *A*. As demonstrated in Figure 2.4c, the U^*_{sum} index is defined as:

$$U^*_{\mathrm{sum}} = U^*_1 + U^*_2 \tag{2.11}$$

As can be seen in Equation 2.11, U^*_1 is the indicator of the internal stiffness between an arbitrary point and the loading point while U^*_2 stands for the internal stiffness between an arbitrary point and the supporting point. The U^*_{sum} index represents the combination of the internal stiffness of an arbitrary point in the structure with both the loading and the supporting points. Consequently, a structure with perfect stiffness distribution should have homogeneous U^*_{sum} distribution. In such a structure, each part would equally contribute to the function of the load transmission. This avoids any excessive usage of material for achieving required structural stiffness.

Based on the above discussion, the homogeneity of the U^*_{sum} distribution can be applied as a design criterion for evaluating the weight-efficiency of load bearing structures. For example, a 1-dimensional spring with the ideal weight-efficiency has a homogenous U^*_{sum} distribution as shown in Figure 2.5a. The degree of homogeneity of the U^*_{sum} index can be

also assessed by the use of a histogram as shown in Figure 2.5b. The weight-efficiency of a structure can be improved through increasing the degree of homogeneity of the U^*_{sum} distribution.

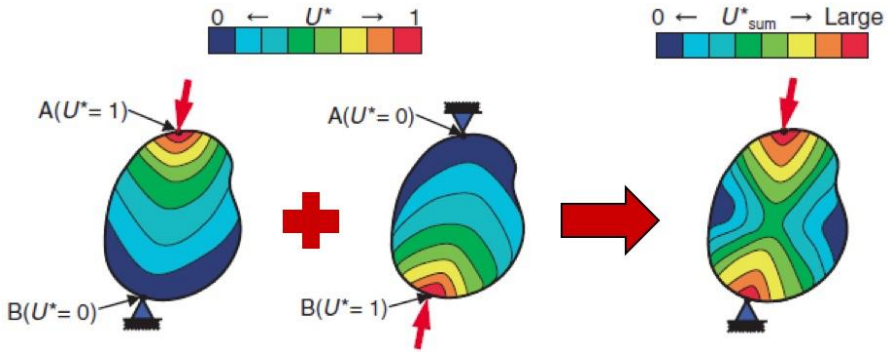

(a) (b) (c)

Figure 2.4: Illustration of U^*_{sum} index- a): Distribution of U^*_1; b): Distribution of U^*_2; c): Distribution of U^*_{sum} .

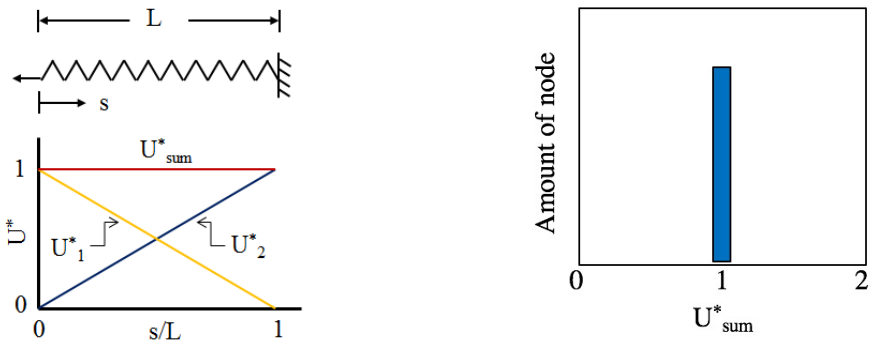

(a) (b)

Figure 2.5: U^*_{sum} index of an ideal structure- a): U^*_{sum} distribution of a spring; b): Histogram of U^*_{sum} index.

2.4 Computer programming for U* calculation

In this thesis, an in-house FEA based program was developed for U^* calculation using Ansys Parameter Design Language (ANSYS 2014). Figure 2.6 shows the logic and the

procedure for the U^* algorithm development. The first step is the calculation of the total strain energy of the original system as shown in Figure 2.1a. Secondly, by fixing an arbitrary node of the system and applying the same displacement to the loading point, the total strain energy of the modified system (see Figure 2.1b) is calculated. Then, the U^* value of the arbitrary node can be computed through Equation 2.6. By repeating this step for each node of the system, the U^* distribution of the whole system is obtained. The total strain energy of the original system is only calculated once.

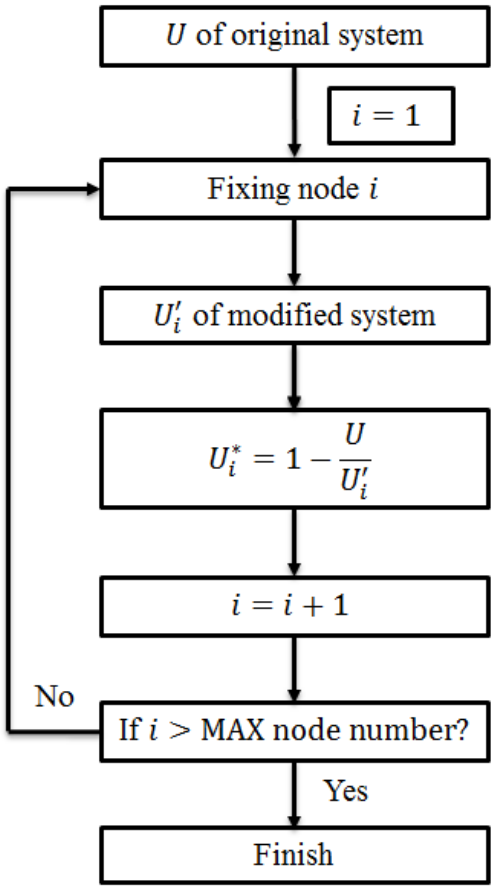

Figure 2.6: Flowchart of the algorithm development for U^* calculation.

2.5 Summary

The objective of the thesis is to improve the original U^* index theory. In this chapter, the concept, the formulation, and the algorithm development of the original U^* index has been presented as the theoretical foundation of the whole thesis. Furthermore, the chapter has elaborated three design criteria (Uniformity, Continuity, and Consistency) and the U^*_{sum} index which are derived from the original U^* index. The introduced design criteria and the U^*_{sum} index will be utilized for structural analysis and modification in the following chapters of the thesis.

Chapter 3

Experimental Validation of the U* Index Theory

3.1 Objective of the experiment

In this chapter, a physical experiment is presented for validating the U^* index theory. The U^* index theory states the route with the highest U^* values transfers the main portion of the force. Therefore, the objective of the experiment is to demonstrate the validity of the above statement. In other words, it is to validate that the line connecting the highest U^* values is indeed the main load path. At the same time with this testing, another experiment was performed under the similar purpose by another group member in author's laboratory (Pejhan et al. 2017b). That testing analyzed the load transfer behavior of a beam system while the experiment in this thesis focused on the load paths of a plate structure.

3.2 Experimental model and procedures

Testing of the load path is the most difficult part of the experiment, because there are no existing facilities or tools that can measure the load path within a continuous structure.

Instead, the measurement of the reaction forces at the supporting points of the structure is more feasible. Accordingly, a desired experimental model should have the following characteristics. Firstly, the reaction forces at the supporting points of the structure should be different. This difference should be relatively larger because the sensor might not be sensitive enough to the small difference between the reaction forces. Then, the load path with the structure should be explicit when the reaction forces are measured. To satisfy the above requirements, an aluminum plate with longitudinal grooves and stiffeners was designed for this experiment. The structure, which is shown in Figure 3.1, has symmetrical grooves and stiffeners on both sides. This characteristic ensures the transferred forces through the grooves and the stiffeners are quite different. If the largest reaction force was measured at the supporting point corresponding to the stiffeners, the main load would be transferred through the stiffeners.

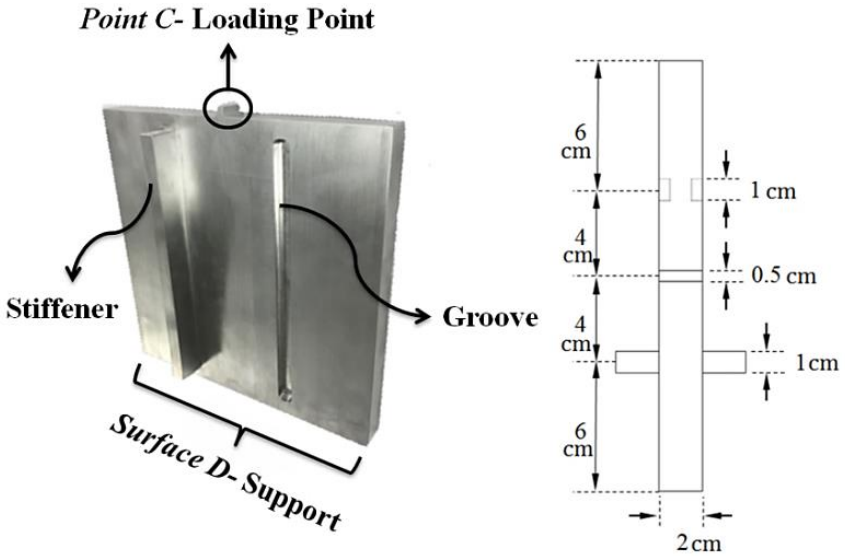

(a) (b)

Figure 3.1: Design of the testing specimen- a): The testing specimen; b): The top view of the experimental model.

The testing specimen is shown in Figure 3.1 together with its dimensions. This testing specimen contained a small step on one side, marked as *Point C* in Figure 3.1. This point was the loading point in this experiment. The other side of the plate, marked as *Surface D* in Figure 3.1, served as the supporting surface of the plate and passed the imposed force to a pressure mat that was placed beneath the test specimen.

The testing procedure for this experiment started by placing *Surface D* of the test specimen on a pressure mat and applying a vertical load on *Point C*. The loading procedure was executed using a MTS Insight electromechanical loading machine (MTS 2014). The loading capacity of the loading machine was 30 KN and it was used to apply a 130 N compressive load on *Point C*. To verify the repeatability of the experiment, loading was removed from the test after gathering data and the process was repeated again. This procedure was performed five times in total.

The measured data in this experiment was the vertical reaction force at the supporting surface (*Surface D*). To measure the reaction forces at different locations of this continuous structure, a FSA SoftFlex pressure mat made by VISTA Medical (VISTA 2014) was used. This pressure mat can record vertical force and is consisted of 256 cells in a 16×16 arrangement. Each cell is 6.45 cm^2 and the sampling rate of the cells is 25 Hz. With a 12-bit resolution, cells have a reading-width of 0 to 300 mm-Hg. The *Surface D*, which was placed on the pressure mat, was 20 cm long. As a result, every 2.5 cm of this surface was located on one cell in the pressure mat and the reading of each cell was recorded on a computer. Figure 3.2 shows a schematic overview of this experiment setup.

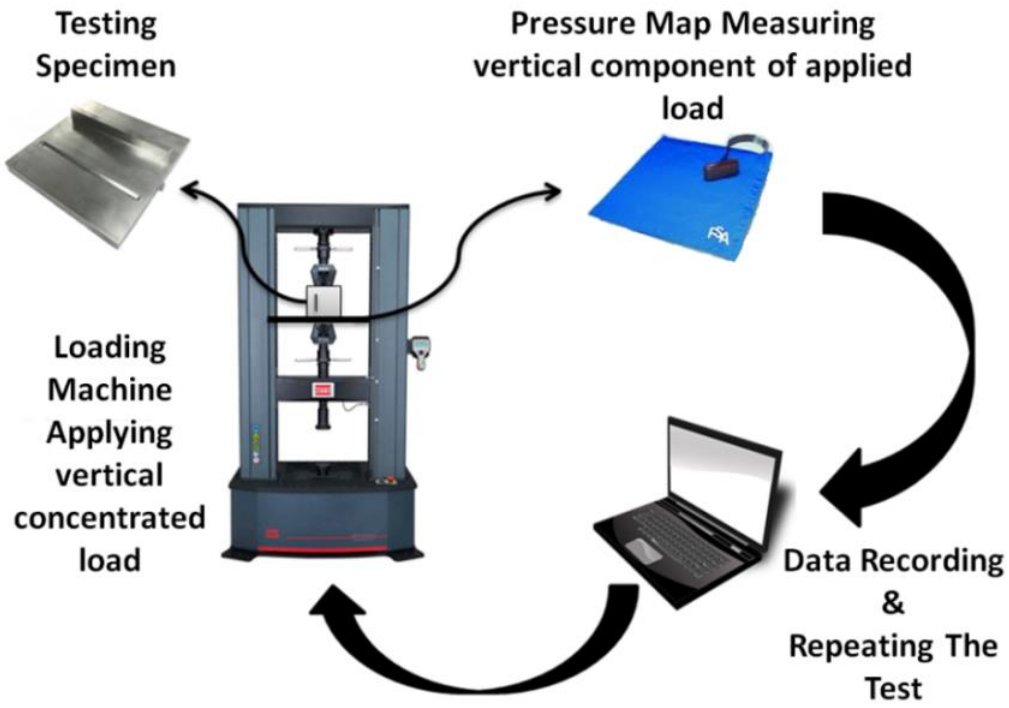

Figure 3.2: Schematic diagram of the testing procedure.

3.3 Results

In this part the experimental result is compared with the computational result in order to see if the U^* index can predict accurate load paths. In the experiment, the bottom of the testing specimen was covered by eight cells of the pressure mat. The measured reaction forces along with the standard deviations and the corresponding locations of the testing specimen are shown in Figure 3.3. Clearly, the stiffener carried a higher amount of load than any other part in the structure. It transferred 48% more load in comparison to the groove and around 36% more than the average load measured by all other cells.

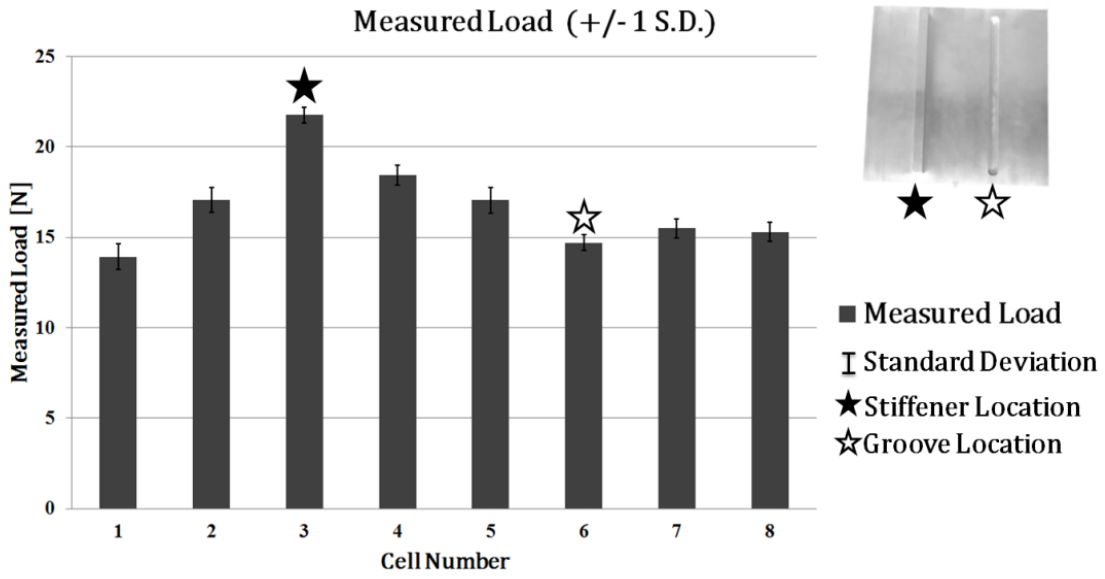

Figure 3.3: Measured reaction forces from the physical testing.

Figure 3.4a elaborates the load paths calculation of the experimental model based on the U^* index. The same loading and supporting conditions in the testing were applied to the finite element model of the testing specimen. From the U^* distribution shown in Figure 3.4a we can see that the main portion of the applied force is transferred along the stiffener. This conclusion is well agreed with the result obtained from the physical testing. Figure 3.4b depicts the U^* distribution of a plate without grooves and stiffeners. Although the main load passes through the middle line of the structure, the distribution of the transferred forces is more uniform than the model with grooves and stiffeners. This means the reaction forces at the supporting points of the structure shown in Figure 3.4b are similar. Thus, the structure without grooves and stiffeners is not suitable for the physical testing due to the small difference between the reaction forces. The results presented by Figure 3.4a and 3.4b

also demonstrate the U^* index is sensitive with the changes of the structural stiffness and can always provide the reasonable load paths.

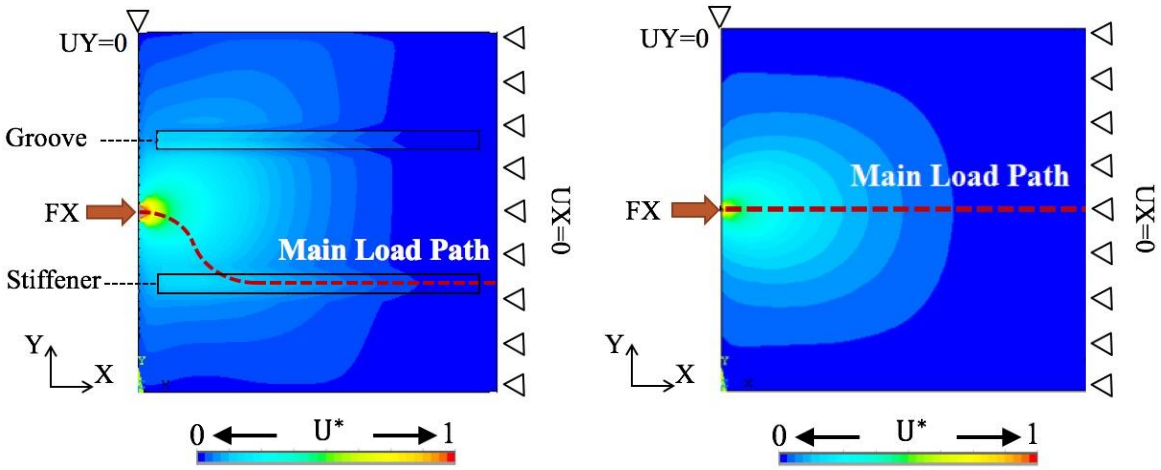

Figure 3.4: Load paths analysis from the U^* index for- a): The experimental model; b): A plate without grooves and stiffeners.

As a comparison, the stress analysis of the experimental model is shown in Figure 3.5a and 3.5b. Figure 3.5a shows the von Mises stress distribution of the structure while Figure 3.5b illustrates the stress values along the grooves and the stiffeners. The results indicate the groove is subjected to the higher stresses than the stiffener. However, the grooves were playing a less significant role in load transfer process as observed in the physical testing. The case study shows the phenomenon of the stress concentration gives misleading information for load transfer analysis. This is a clear example of the advantage of using the U^* index theory for load transfer analysis in comparison to stress trajectory based methods.

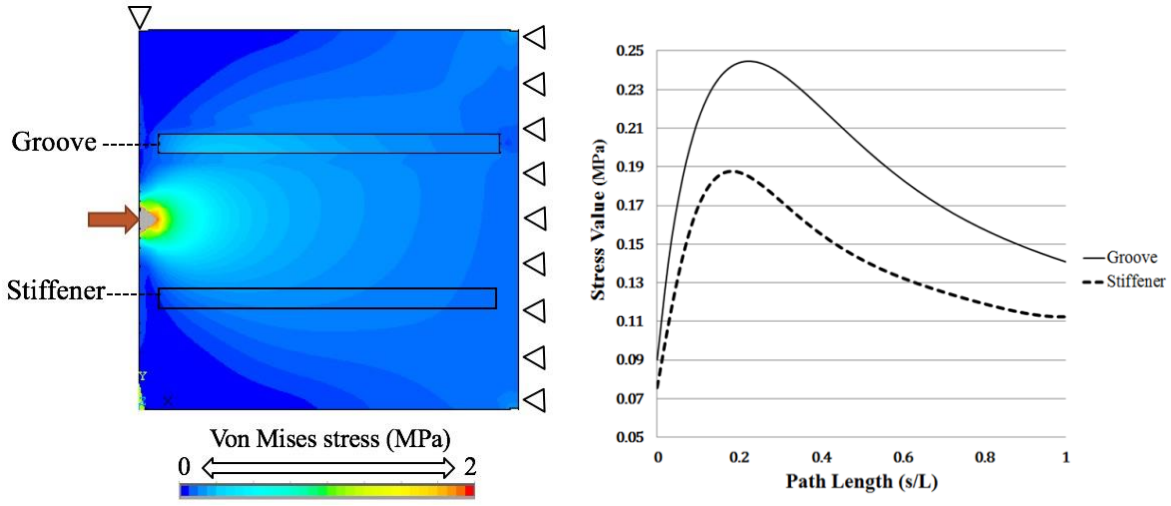

(a) (b)

Figure 3.5: Stress analysis of the testing model- a): Distribution of the von Mises stress; b): The stress values along the groove and the stiffener.

Based on the results of this experiment, it can be stated that the main load path for transferring the proposed loading in this structure starts from the loading point, passes through the stiffener and ends up in the cell below the stiffener. This conclusion is in complete consistency with the load path determined by U^* index simulation and proves that U^* index theory is capable of identifying load paths to continuous structures. In addition, the conventional stress analysis performed on the model reveals that the application of the U^* index theory for load transfer analysis, instead of stress based load path analysis, is much more reliable for finding the load transfer path. Although the groove is not the main load carrier as shown in the experiment, the stress analysis predicted high stress values in the groove due to the geometrical singularity. Consequently, the stress trajectory method for finding the load path cannot be trusted because of these local geometrical irregularities.

The presented results have been published in (Pejhan et al. 2017b) together with another validation experiment.

3.4 Summary

In the presented study, the physical validation experiment for the U^* index theory was proposed and tested successfully. This theory has achieved a growing attention in the automotive engineering and by using the suggested test setups, it was shown that the U^* index is an adequate measure for load transfer in a structure. The agreement between the testing and the numerical calculation proves that the U^* index is capable of predicting the load path and load transfer behavior of the structure and it can also be trusted to follow real changes in the load path due to structural variations without falling for the effects of stress concentration.

Chapter 4

Demonstration of the Effectiveness of the U^* Based Design Criteria

The objective of this chapter is to demonstrate the effectiveness and the capability of the U^* related design criteria for improving the structural performance and efficiency. In this chapter, a revised design of a vehicle component was proposed based on the U^* driven design criteria. The structural improvement in terms of the U^* based design criteria is presented. In the meantime, the performance and the weight-efficiency of the sample structure are significantly raised through the design modification. Compared to the original design, the revised structure is 10% lighter while the maximum structural displacement and stress are decreased by 5% and 26% under the same loading, respectively. The results prove that the application of the U^* driven design criteria can effectively increase the structural performance.

4.1 Design modification

The sample structure for the design modification is a parcel rack strut from a bus as shown in Figure 4.1a. The strut has the length of 640 mm, the height of 320 mm, and the

width of 73 mm. A simplified computer model of the strut is presented in Figure 4.1b. As illustrated in Figure 4.1b, the computer model is fully constrained at the aisle ceiling and outside mounts and loaded at the middle of the horizontal section of the strut with vertical forces towards to the floor of the bus. This vertical loading is used to simulate the main service loading of the strut coming from the parcels of passengers. The material properties of the strut and the magnitude of the service loading are displayed in Table 4.1.

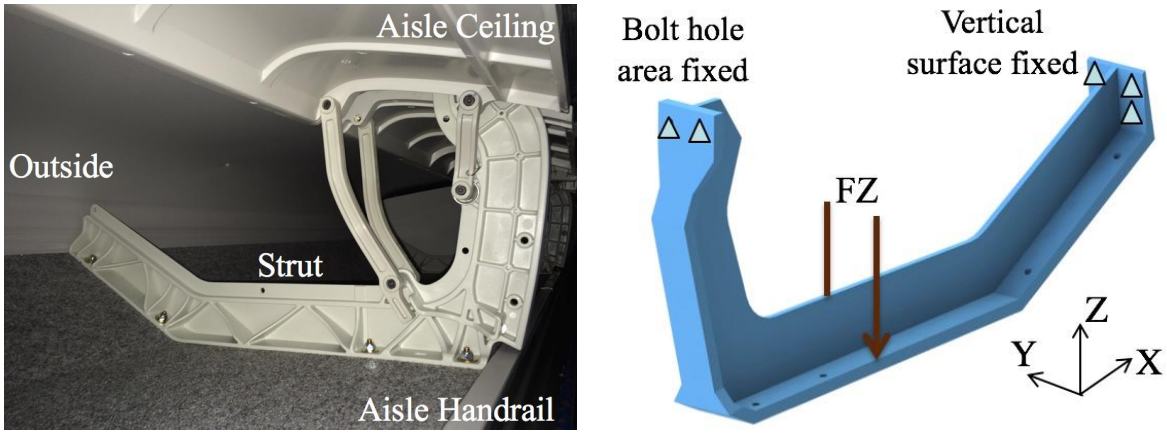

(a) (b)

Figure 4.1: Sample structure for design modification- a): The parcel rack strut in a bus; b): The computer model and the boundary conditions.

The design modification of the strut is conducted to address the loading condition shown in Figure 4.1b. The objective of the design modification is to improve the structural performance and the weight-efficiency without affecting the structural function. Based on the U^* governed design criteria, three structural issues were detected for the parcel rack strut. The first one happens to the vertical part of the structure. Figure 4.2a depicts the U^*_2 variation along the left edge for the vertical part of the strut. A rapid decay of the U^*_2 index

occurs at the marked area of the strut. The phenomenon reveals the internal stiffness of marked area of the strut is lower than the adjacent areas. The lower internal stiffness may cause the marked area fail earlier since it cannot resist the applied force as well as the adjacent areas. The similar non-uniform U^*_2 decay can be also observed in the marked area of the horizontal part of the strut as shown in Figure 4.2b. Both of the issues are caused by the bent sections of the strut. In order to improve the uniformity of the internal stiffness distribution in the structure, the curvatures of the bent sections should be enlarged. However, those structural issues can hardly be identified based on the stress values (see Figure 4.8a).

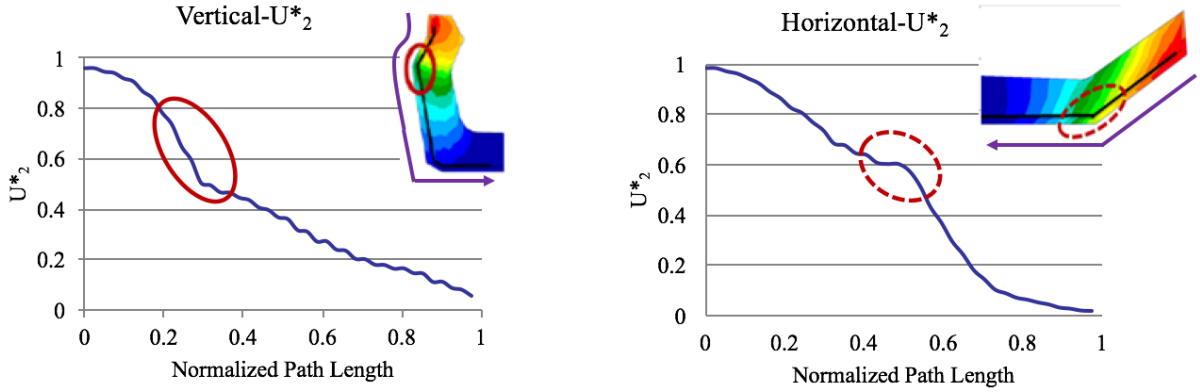

(a) (b)

Figure 4.2: U^* variation of the strut along- a): Left edge of the vertical section; b): Bottom edge of the horizontal section.

The third issue is detected through the U^*_{sum} index. In an efficient structure, the values of the U^*_{sum} index in the whole structure should be consistent as introduced in Chapter 2.3. As a sequence, the distribution of U^*_{sum} was calculated for the parcel rack strut. It can be seen in Figure 4.3a that the U^*_{sum} values of Segment *A* and Segment *C* are higher than other

segments, which suggests these two segments have higher internal stiffness. The internal stiffness of those segments should be reduced in order to raise the homogeneity of the U^*_{sum} distribution of the whole structure. Reducing the material is an effective way to lower down the internal stiffness in Segment *A* and Segment *C*. Adding material to the segments with lower U^*_{sum} index can also improve the homogeneity of the U^*_{sum} index. However, it is not recommended because adding material to segments deviated from the main load paths can degrade the structural efficiency. It is worth to mention that the stress values shown in Figure 4.8a cannot predict any segment of the strut which is suitable for material reduction.

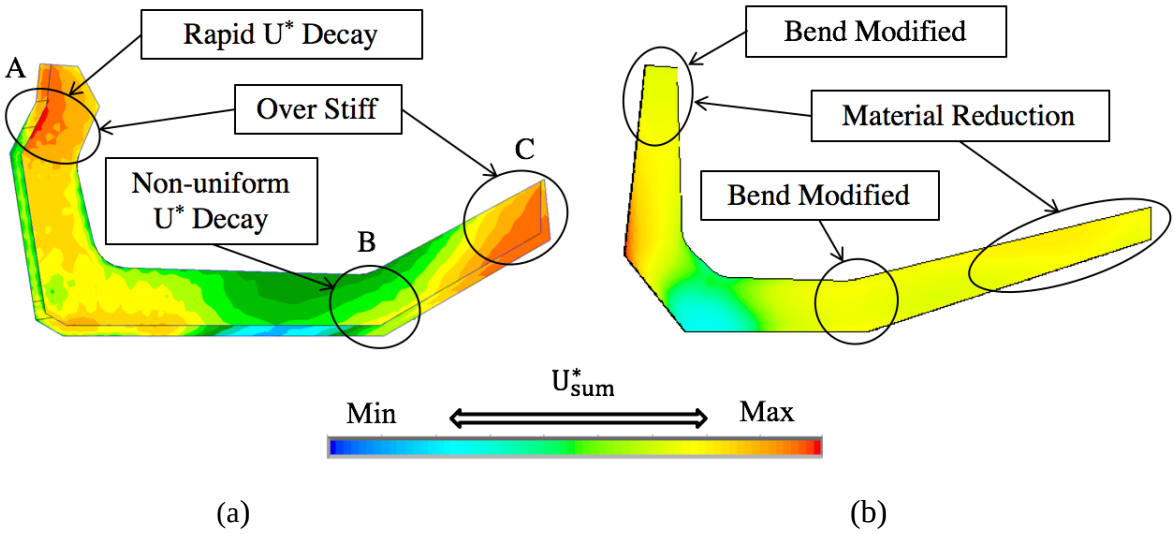

Figure 4.3: Structural modifications and U^*_{sum} distributions- a): U^*_{sum} distribution of the original strut and the structural issues; b): U^*_{sum} distribution of the modified strut and the design modifications.

The three structural issues of the strut are summarized in Figure 4.3a, while the corresponding modifications to the strut are presented in Figure 4.3b. To be more specific, the bend of the Segment *A* was modified to be straight and the curvature of the bend of

Segment *B* was enlarged. Meanwhile, the thickness of Segment *A* and Segment *C* was decreased. To ensure the revised strut has the same utility as the original, the overall dimensions (height, length, and width) of the strut are kept constant during the structural modifications.

4.2 Results

This section presents the results of the design improvement to the parcel rack strut. The results of the design improvement of the parcel rack strut are presented from the viewpoints of both the U^* index and the maximum displacement and stress. The design modifications were obtained based on the U^* driven design criteria. As a result, the improvement should be seen from the viewpoint of the corresponding U^* driven design criteria.

U^* Uniformity

As introduced in Chapter 2.2, the uniformity of the U^* variation is used to evaluate the rationality of the stiffness distribution of the structure. Compared with the original strut, the revised strut performs better in terms of the U^* Uniformity. As shown in Figure 4.4a, the U^*_2 variation along a specific path on the left edge of the revised strut is depicted by the solid line, where the dashed line represents the corresponding U^*_2 variation of the original strut. Same pattern can be observed with respect to the horizontal part of the strut in Figure 4.4b. It can be seen from Figure 4.4a that instead of the sharp decline the U^*_2 index in the marked segment of the vertical part of the strut is uniform. In the horizontal part of the strut, as shown in Figure 4.4b, the U^*_2 variation of the revised structure is more uniform compared with the original design. Consequently, the stiffness distribution of the revised

strut is more acceptable. The overall stiffness of the strut is increased as can be seen from Figure 4.7b.

In this study, the modification was made to the strut in light of the detected U^* non-uniformity. The usefulness of the design criterion was well demonstrated through the design modification. The work also shows that quantitative evaluation of the U^* non-uniformity would be helpful for decision making, though it was not provided in this preliminary stage of the study on the U^* based design criteria. In Chapters 6 and 7, the approaches to quantitative analyses of the U^* based design criteria are presented.

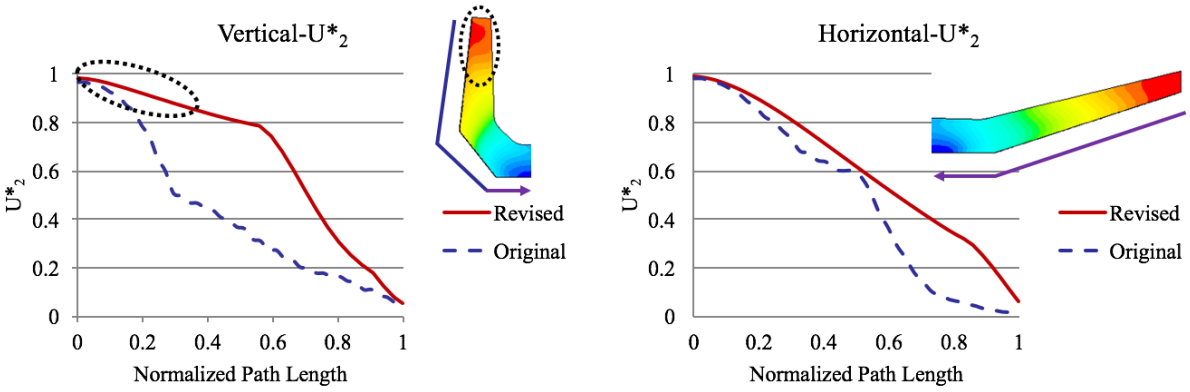

(a) (b)

Figure 4.4: The comparison of U^* variations between the revised (solid line) and original (dashed line) struts in- a): The vertical section; b): The horizontal section.

U^*_{sum} Homogeneity

Another criterion, which can evaluate the structural efficiency is the homogeneity of the U^*_{sum} index. The histograms of the U^*_{sum} index in the original and the revised struts are presented in Figure 4.5a and Figure 4.5b, respectively. It can be seen from the histograms that the degree of homogeneity of the U^*_{sum} index in the revised design is much higher than

that of the original strut. The high homogeneity of the U^*_{sum} index demonstrates most components of the revised strut have the similar significance in the function of load transfer. It also proves that efficiency of the structure is raised by the design modifications. Same conclusion can be drawn when comparing the contour plots of the U^*_{sum} distributions in the original (Figure 4.3a) and the revised struts (Figure 4.3b).

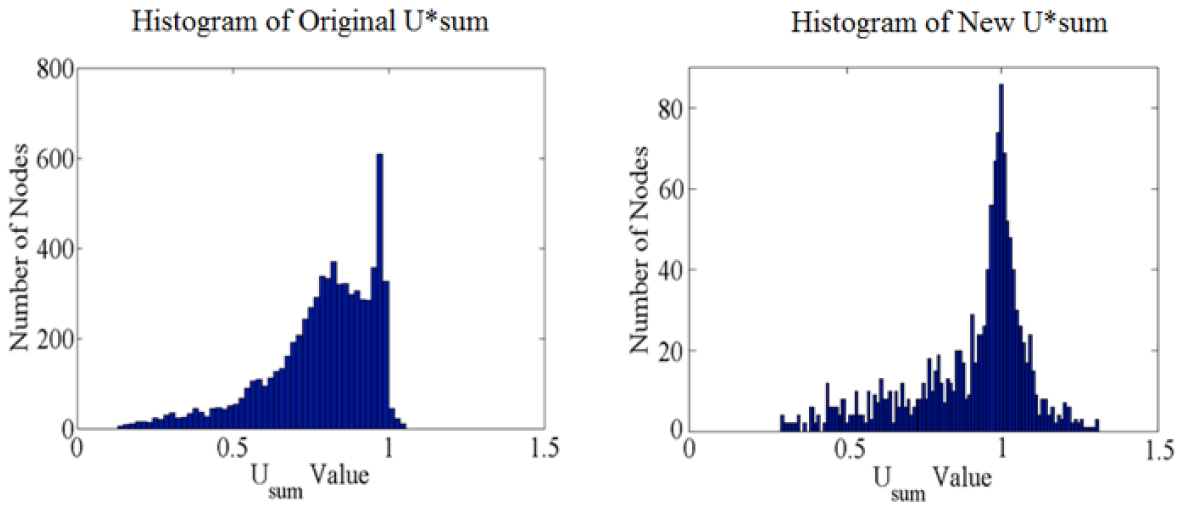

(a) (b)

Figure 4.5: Histograms of the U^*_{sum} index of- a): The original strut; b): The revised strut.

Load Paths Consistency

Compared with the original design, the revised strut is also improved in terms of the design criterion "Consistency". Consistency demands that a desirable structure should have a good consistency between the load path of the applied force (predicted by the index U^*_1) and the load path of the reaction force (calculated by the index U^*_2). It can be seen in Figure 4.6a that the load paths in the horizontal part of the original strut are coincident with each other, whereas the load paths in the vertical part are quite different. In contrast, the

load paths of the revised strut are consistent with each other perfectly in both the vertical and the horizontal parts, which can be seen in Figure 4.6b. This indicates the revised strut is more efficient than the original one in the force transmission.

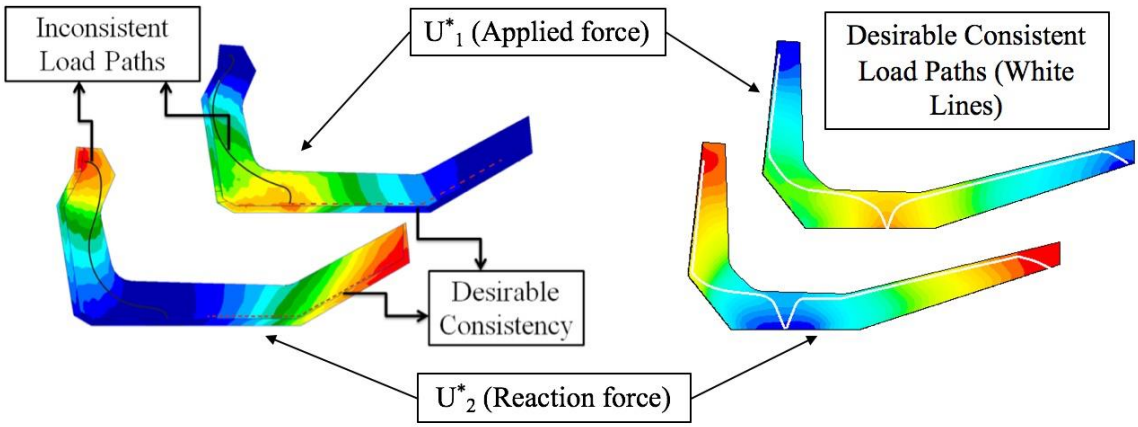

Figure 4.6: The consistency between the load paths of the applied force and the reaction force of- a): The original strut; b): The revised strut.

Table 4.1: The computational data of the struts

Model	Material	Mass (g)	Service Loading (N)	Maximum Displacement (mm)	Maximum von Mises Stress (MPa)
Original Strut	Nylon	1,403	1,921	2.49 (horizontal section)	20.6 (upper neck)
Modified Strut		1,265		2.37 (horizontal section)	15.2 (upper neck)

The final goal of the proposed design modifications is to increase the structural performance. In this section, the maximum displacement and stress are used to evaluate the structural performance. It can be seen from Table 4.1 that the mass of the revised strut (1265 grams) is 10% lighter than the original strut (1403 grams). Furthermore, the

maximum displacement of the revised strut is 5% smaller compared to the original strut. The total displacements of the original and the revised struts were shown in Figure 4.7a and Figure 4.7b, respectively. Meanwhile, the maximum stress (15.2 MPa) of the revised strut (see Figure 4.8b) is 26% lower than the original strut (see Figure 4.8a). The computations of the revised strut are under the same loading and supporting conditions as the original strut (see Figure 4.1b).

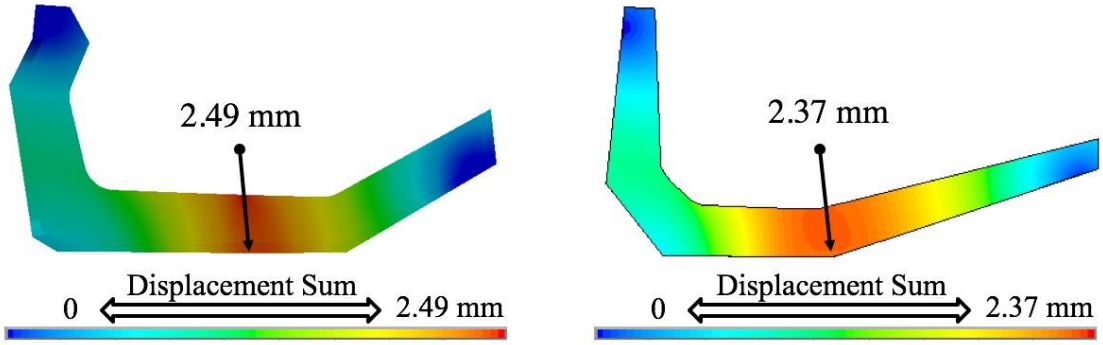

(a) (b)

Figure 4.7: Displacement sum of- a): the original strut; b): the revised strut.

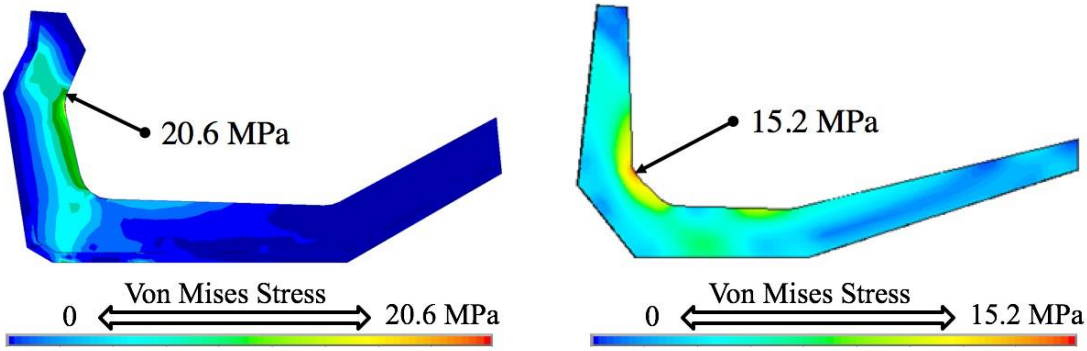

(a) (b)

Figure 4.8: Von Mises stress of- a): the original strut; b): the revised strut.

4.3 Summary

In this chapter, design modifications were carried out to a parcel rack strut based on the U^* driven indices and design criteria. Compared to the original structure, the weight of the revised structure is decreased by 10% while the overall stiffness of the strut is increased by 5%. Meanwhile, remarkable improvements can be observed in the revised strut from the uniformity of the U^* index, the consistency of the load paths, and the homogeneity of the U^*_{sum} index. The results of the redesign of the strut demonstrate the U^* theory including the U^* related indices and design criteria is an effective tool in structural design modifications. The improvements of the structure from the viewpoint of the U^* index can lead to the increase of the structural efficiency and performance.

The homogeneity of the U^*_{sum} index can be used to evaluate the weight-efficiency of the structure. A desirable structure should have an equal U^*_{sum} value throughout the whole structure. Reducing the material from the parts with higher U^*_{sum} values is an effective way to improve the degree of the homogeneity of the U^*_{sum} distribution.

The non-desirable stiffness distribution of the structure can be identified using the Uniformity of the U^* index. The increase of the U^* Uniformity can result in the enhancement of the overall stiffness of the structure.

The Consistency between the load paths of the applied and the reaction forces can reflect the improvements of the structural efficiency and performance from another point of view. As the promotion of the structural efficiency and performance, the load paths of the applied and the reaction forces are consistent with each other instead of the deviation.

Compared to the stress analysis, the U^* index theory can provide designers with additional information in vehicle structural design evaluation and modification. The combined utilization of both U^* index and stress analysis is an effective and efficient way to achieve better vehicle structures.

Chapter 5

Extensions of the U^* Index Theory to Orthotropic Materials and Six DOFs Systems

The original U^* index theory assumed the material as isotropic, therefore it is not valid for composite materials which are anisotropic. Meanwhile, the original U^* index theory derived from the mechanical system conforms to three DOFs neglecting the rotational DOFs. As a result, it is inapplicable where six DOFs are needed. In this chapter, two new load transfer indices (U^*_O and U^*_M) are proposed to extend the U^* index theory into mechanical systems with orthotropic materials and six DOFs, respectively.

5.1 U^*_O index for orthotropic materials

Composite materials are essential for lightweight structures due to their high specific strength (30-40% lighter than steel with same strength). The weight-efficiency of the composite structure could be further increased by an appropriate reinforcement along its main load path. Therefore, a means to perform load transfer analysis of composite materials is imperative to the engineering community.

5.1.1 U^*_O index for orthotropic system

A main difference between isotropic materials and composite materials is the elastic modulus. For isotropic materials the elastic modulus is constant in all directions, while for composite materials the elastic modulus varies with the direction. As shown in Figure 5.1a, the composite model is assumed as linear elastic, orthotropic, and homogenous coming with the loading point *A*, the supporting point *B*, and an arbitrary point *C*. In the orthotropic system, 1-direction is the longitudinal direction of the fibers, which is perpendicular to the 2-direction. The arrow pointing from point *A* to point *C* is denoted as the *x*-direction. θ is the off-axis angle of *x*-direction with respect to 1-direction (fibre direction). The specifications of the constants of the composite material are presented in Table 5.1.

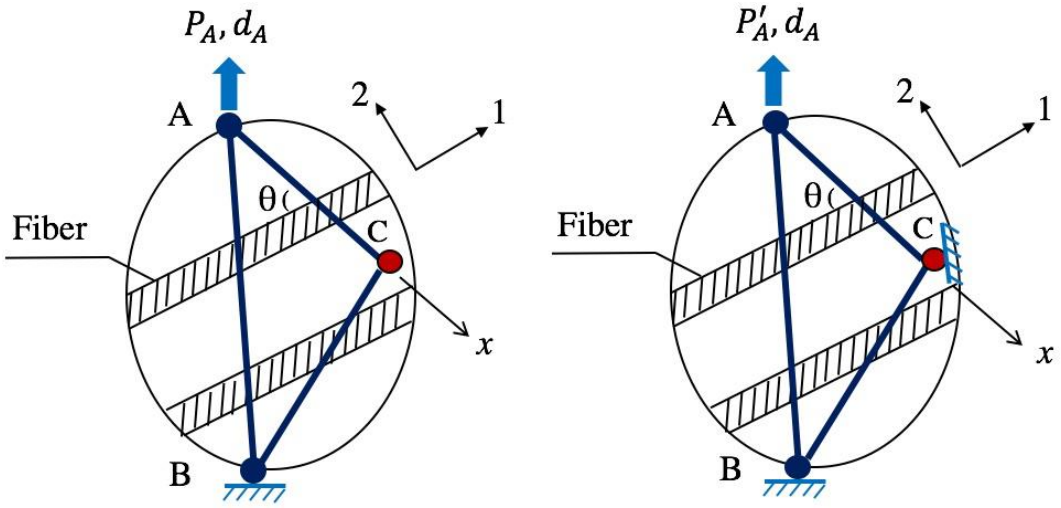

(a) (b)

Figure 5.1: Orthotropic system for U^*_O calculation- a): Original system; b): Modified system.

Table 5.1: Specifications of the material constants for the orthotropic system

	Specifications		Specifications
E_1	Elastic modulus in longitudinal direction of fibers	G_{12}	In-plane shear modulus
E_2	Elastic modulus in transverse direction of fibers	v_{12}	Major Poisson's ratio

The load transfer behavior of the composite material is highly affected by the fibers. Hence, to predict accurate load paths for composite materials, it is necessary to construct the relationship between the load transfer index (U^*_O) and the fiber direction. As illustrated in Figure 5.1a, instead of the springs (see Figure 2.1a), the beams stand for the internal stiffness between any two points in the orthotropic system. The use of the beams here is just to ensure the clearness and distinctness of the fibers and the angle between line *AC* and the fibers. The elastic modulus of the orthotropic system in *x*-direction, i.e. E_x, conforms to (Jones 1998)

$$\frac{1}{E_x} = \frac{\cos^4\theta}{E_1} + \left[\frac{1}{G_{12}} - \frac{2v_{12}}{E_1}\right]\sin^2\theta\cos^2\theta + \frac{1}{E_2}\sin^4\theta \tag{5.1}$$

where E_x is a function of θ i.e., $E_x = E_x(\theta)$. Since the (internal) stiffness linearly depends on the elastic modulus (E_x) (Beer et al. 2006; Pejhan et al. 2017b; Takahashi 1986), K_{AC} can be also written into a function of the angle θ i.e., $K_{AC} = K_{AC}(\theta)$. Based on Equation 5.1, E_x is inversely proportional with the angle θ. Hence, the internal stiffness K_{AC} is inversely proportional with the angle θ as well. An example of the relationship between the elastic modulus (E_x) and the angle θ of a typical unidirectional fiber composite is shown in Figure 5.2.

The U^*_O index is defined as:

$$U_O^* = 1 - \frac{U_O}{U_O'} \tag{5.2}$$

where U_O is the total strain energy of the orthotropic system with unrestrained point *C* (see Figure 5.1a) and U_O' is the total strain energy of the orthotropic system when point *C* is restrained (see Figure 5.1b). Following the same computational procedures of the basic U^* index (Equation 2.1~2.7), the U^*_O index can be written into the form:

$$U_O^* = \left[1 - \frac{2U_O}{(\boldsymbol{K_{AC}}(\boldsymbol{\theta})\boldsymbol{d_C}) \cdot \boldsymbol{d_A}}\right]^{-1} \tag{5.3}$$

As can be seen from Equation 5.3, the proposed U^*_O index is still only related with the internal stiffness between the loading point and an arbitrary point of the composite structure. Meanwhile, it varies with the angle (θ) between *x*-direction and the fiber direction, which makes this index sensitive with the fiber direction of the composite structure. The U^*_O index is inversely proportional with the angle θ. The difference between the new U^*_O and the original U^* indices is that the U^*_O index considers θ as a parameter to affect the internal stiffness while the original U^* index does not. As a result, the new U^*_O index is expected to predict accurate load paths of composite structures. It is worth to mention that the proposed U^*_O index is a universal form for both isotropic and orthotropic materials. If materials were considered as isotropic, the angle θ would not affect the U^*_O index any more. In this situation, the expression of the U^*_O index will be same as the original U^* index.

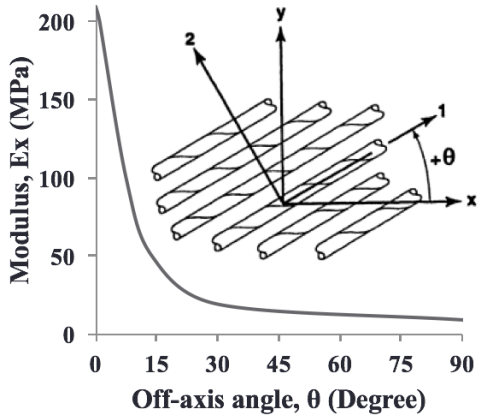

Figure 5.2: Elastic modulus of a typical composite material (Jones 1998).

To demonstrate the relationship between the U^*_O index and the angle θ, the U^*_O index was calculated for a composite structure described in Figure 5.3. Two symmetrical points of the structure are fully constrained. Since the fiber of the structure is symmetrically distributed, the Poisson's contraction in *X*-direction does not affect the load transfer in *Y*-direction. For comparison purposes, the material of the structure was assumed as isotropic in the first set of the calculation while it was considered to be orthotropic in the second set of calculation. Figure 5.4a and Figure 5.4b present U^*_O distributions of the isotropic and the orthotropic models, respectively. Figure 5.4c illustrates the variations of the U^*_O index in the direction of the arrow for both isotropic and orthotropic models. It can be seen from Figure 5.4c that the U^*_O index of the orthotropic model drops faster than that of the isotropic model. This phenomenon is due to the effect from the angle θ. As can be seen from Figure 5.3 that the angle θ between *AC*-direction and the fiber increases when point *C* moves along the arrow to point *C'*. In the isotropic model, the elastic modulus is constant with the angle θ, therefore the the angle θ does not affect the U^*_O index. However, in the orthotropic structure, the angle θ

is inversely proportional with the elastic modulus and the internal stiffness. As a result, the influence from the angle θ causes a faster drop of the U^*_O index in the orthotropic model. The result also reveals the original U^* index which assumes the material as isotropic cannot characterize the effect of fibers on the load transfer behavior of the composite structure.

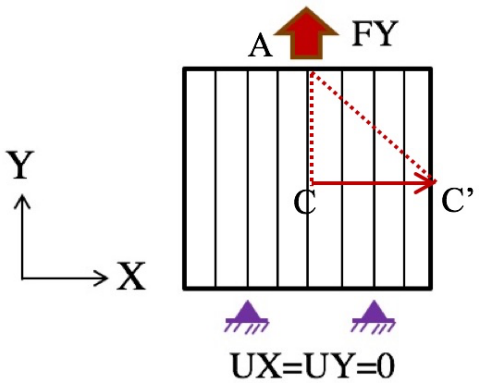

Figure 5.3: Sample structure (solid lines represent fiber) to show the relation between U^*_O and θ.

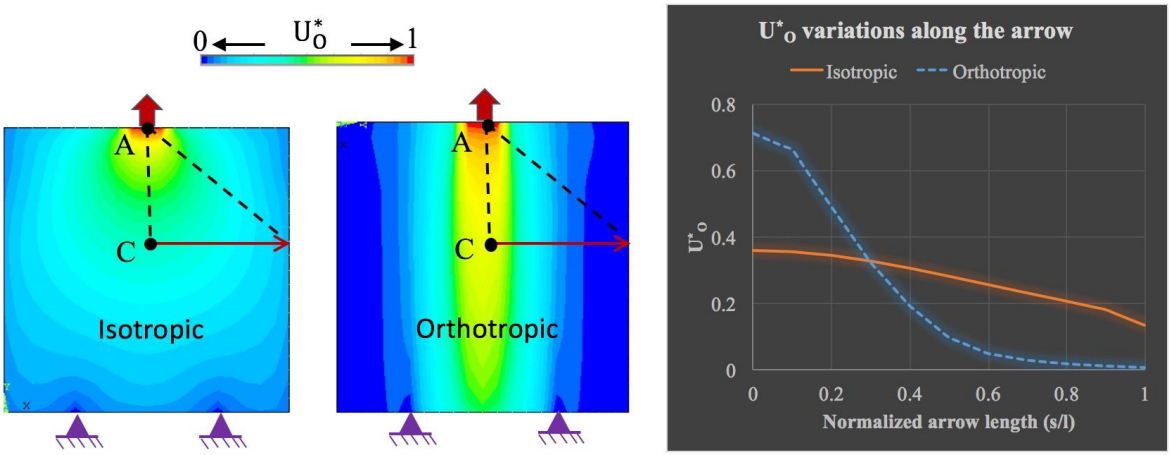

(a) (b) (c)

Figure 5.4: U^*_O distributions of the sample structure- a): The material is assumed as isotropic; b): The material is assumed as orthotropic; c): U^*_O variations along the red arrow.

5.1.2 Case studies in orthotropic composites

To demonstrate the effectiveness of the new U^*_O index in load paths analysis of composite structures, two case studies are carried out in this section on unidirectional and woven fiber reinforced composite, respectively.

Case Study 1: Unidirectional

As shown in Figure 5.5, three different computational models were generated based on a unidirectional carbon fiber epoxy from literature (Jones 1998) with the same dimensions, loading, and boundary conditions. A compression force is applied on the top middle of the structure, while the bottom of the structure is simply supported. As a comparison, the material of the model shown in Figure 5.5a is considered to be isotropic and the basic U^* index is used to analyze the load transfer, while the models displayed in Figure 5.5b and Figure 5.5c which have different fiber directions are assumed as orthotropic and the load paths are determined using the proposed U^*_O index. The material properties of the computational models in Case Study 1 are displayed in Table 5.2.

Table 5.2: Material properties of computational models in Case Study 1

Properties	E(GPa)		G_{12}(GPa)	v_{12}
	E_1(GPa)	E_2(GPa)		
Orthotropic	210	5.25	2.63	0.25
Isotropic	210			0.3

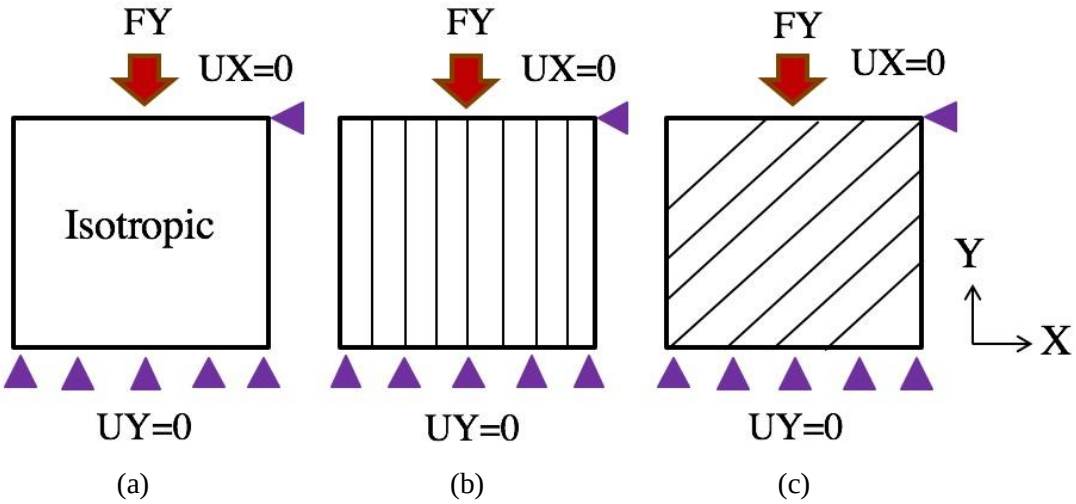

Figure 5.5: Computational models in Case Study 1 (solid lines represent fiber)- a): Isotropic structure, b): $[0]_s$ fiber reinforced composite, c): $[45]_s$ fiber reinforced composite.

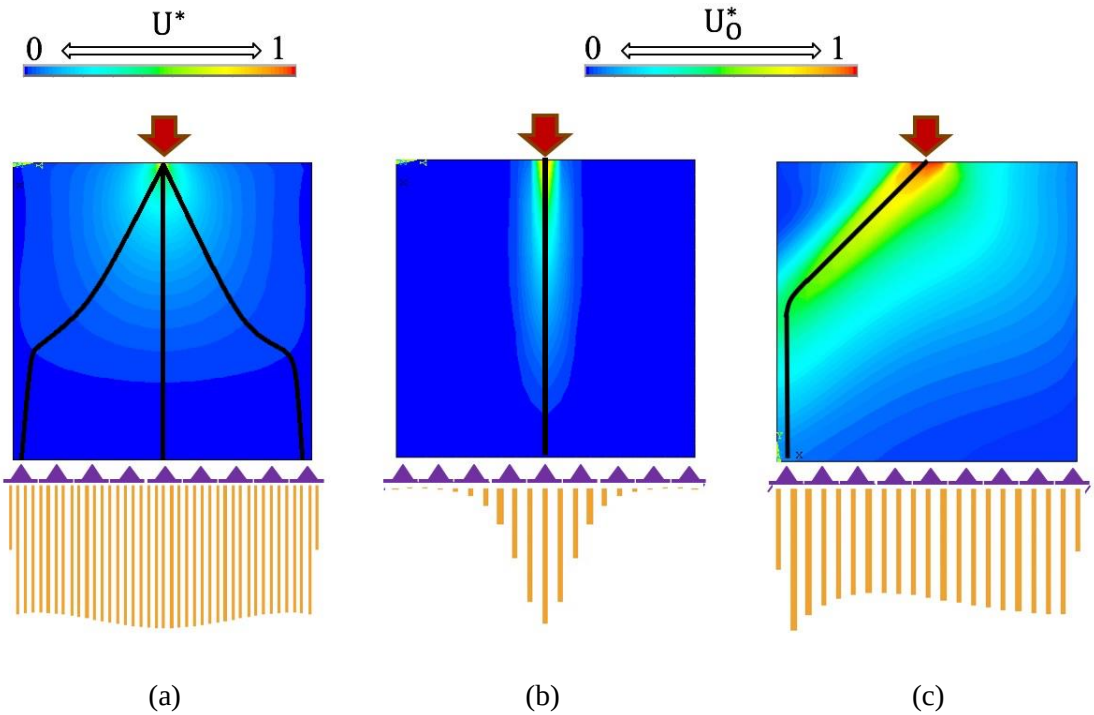

Figure 5.6: The U^* or U^*_O distribution (contours), the main load paths (solid black lines), and the reaction forces (bar charts) for- a): Isotropic structure, b): $[0]_s$ fiber reinforced composite, c): $[45]_s$ fiber reinforced composite.

The computational results of Case Study 1 are shown in Figure 5.6a, Figure 5.6b, and Figure 5.6c, where the contours represent the U^* or U^*_O distributions and the solid black lines depict the main load paths. In composite structures, fibers carry the main portion of the loads instead of the resin. Consequently, the main load paths of the composite structure are supposed to be aligned with the fiber direction. It can be seen from Figure 5.6b and Figure 5.6c that the highest U^*_O values and the resultant main load paths are converged to the fiber directions. As a comparison, the load transfer in the isotropic model is much more uniform, which can be seen from the U^* distribution and the main load paths shown in Figure 5.6a. Another proof for verifying the load paths calculation is the reaction forces of the models, which are indicated by the bar charts in the lower part of Figure 5.6a, Figure 5.6b, and Figure 5.6c. When multiple points are constrained for a load bearing structure, the main load path should reach the supporting point which has the largest reaction force. As can be seen from Figure 5.6, the predicted main load paths of the three computational models all arrive at the points with the highest reaction forces.

Case Study 2: Woven

Another set of computational models was constructed based on a woven glass fiber composite specimen from literature (Ghasemnejad and Hadavinia 2010) with the same dimensions, loading and boundary conditions as shown in Figure 5.7. The composite structures are loaded at the top middle with a concentrated force and simply supported at the bottom. Similar to Case Study 1, the material of model shown in Figure 5.7a remains isotropic, while the materials of the models shown in Figure 5.7b and Figure 5.7c are considered as orthotropic. Table 5.3 presents the material properties of the computational

models in Case Study 2. In the load transfer analyses, the basic U^* index was utilized for the isotropic model, while the proposed U^*_O was applied to the orthotropic models.

Table 5.3: Material properties of the computational models in the case study 2.

Properties	E(GPa)		G_{12}(GPa)	v_{12}
	E_1(GPa)	E_2(GPa)		
Orthotropic	27	26	6	0.14
Isotropic	210			0.3

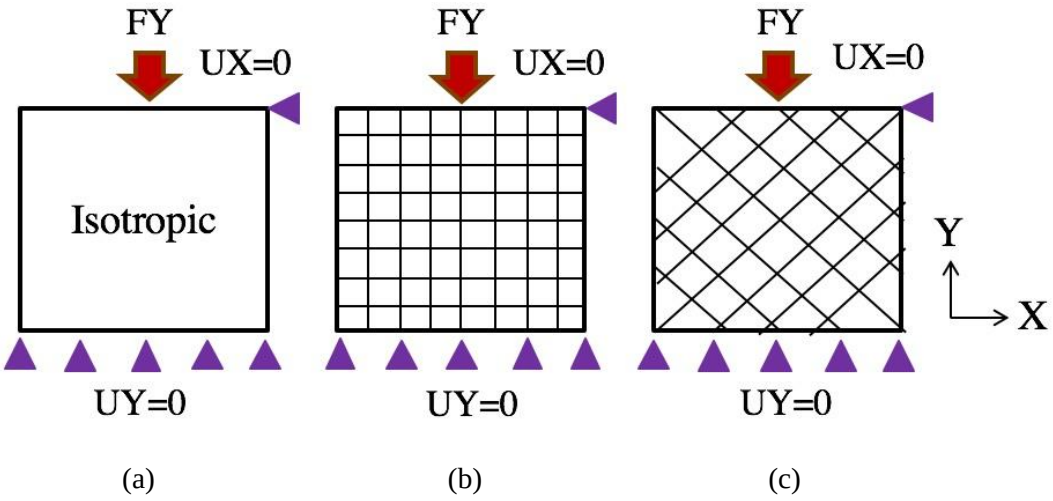

(a) (b) (c)

Figure 5.7: Computational models in Case Study 2 (solid lines represent fiber)- a): Isotropic structure, b): $[0/90]_s$ fiber reinforced composite, c): $[\pm 45]_s$ fiber reinforced composite.

The results of Case Study 2 are presented in Figure 5.8a, Figure 5.8b, and Figure 5.8c, where the U^* or U^*_O distributions are illustrated by the contours and the main load paths are shown by the solid black lines. Meanwhile, the absolute values of the reaction forces for each model are shown by the bar charts in the lower part of the corresponding figures. It can be seen from Figure 5.8b and Figure 5.8c that the resultant main load paths from the

U^*_O distributions still well correlated with the fiber directions of the woven composites. In contrast, the load paths distribution of the isotropic model is more uniform as shown in Figure 5.8a. Furthermore, from the computational results shown in Figure 5.8, good consistency can be observed between the predicted main load paths and the reaction forces in each sample structure.

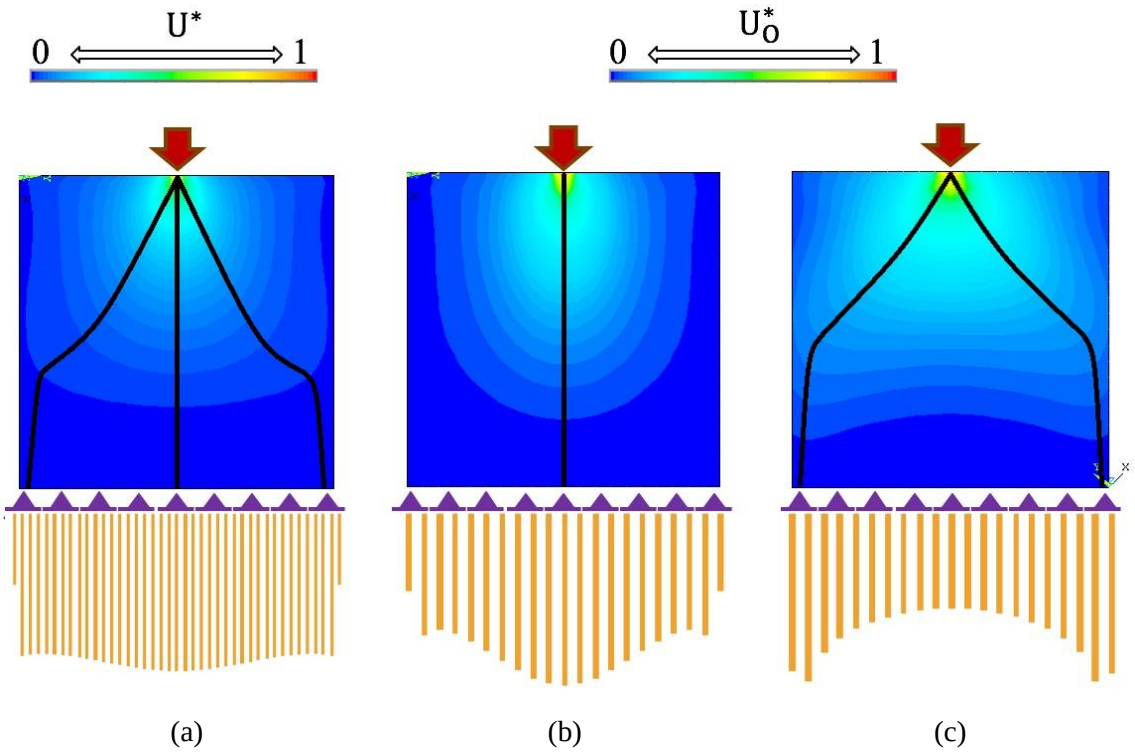

(a) (b) (c)

Figure 5.8: The U^* or U^*_O distribution (contours), the main load paths (solid black lines), and the reaction forces (bar charts) for- a): Isotropic structure, b): $[0/90]_s$ fiber reinforced composite, c): $[\pm 45]_s$ fiber reinforced composite.

It can be seen from the results of Case Study 1 and Case Study 2 that the proposed U^*_O index is able to predict load paths for orthotropic composite structures coming with the consistency with both fiber directions and reactions forces. On the other hand, the performed analysis demonstrates that under the same loading and supporting condition, the

load transfer behaviour of orthotropic structures and isotropic structures are quite different, which can be seen from both Figure 5.6 and Figure 5.8. In other words, if the composite structure was assumed as isotropic, the result of the load transfer analysis would be widely different from the reality. Hence, the isotropic assumption is not recommended for composite structures in load transfer analysis though it makes the computation easier. The presented results have been published in (Wang et al. 2017a).

5.2 U^*_M index under six DOFs systems

The original U^* index was derived based on the three-dimensional continuum theory where the rotational DOFs are not considered. Hence, it cannot be used in the structural analysis where rotational DOFs cannot be neglected. In this section, a new load transfer index (U^*_M) with six DOFs was introduced on the basis of the theoretical foundation of the original U^* index. The new U^*_M index is formulated by considering both three translational and rotational DOFs. The accuracy of the proposed U^*_M index was demonstrated through comparisons with the original U^* index which has been experimentally validated.

5.2.1 Formulation of the U^*_M index

Figure 5.9a shows a force and a bending moment are applied simultaneously to a linear elastic body at the loading point *A* while point *B* of the structure is fully fixed. Since the springs shown in Figure 1a are not capable to provide the internal stiffness when rotational DOFs are involved, beams are used as the representative of the internal stiffness between any two points in the system shown in Figure 5.9a.

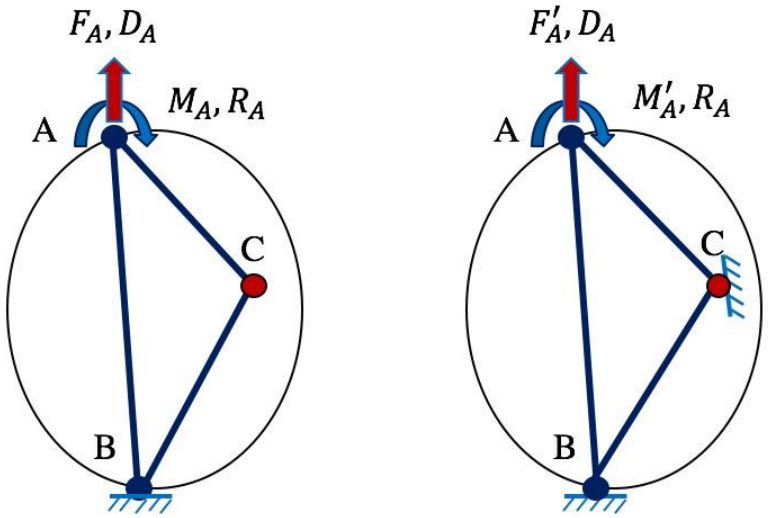

(a) (b)

Figure 5.9: Mechanical model for calculation of the new U^*_M index- a): Original system; b): Modified system.

The force-displacement relationship among points *A*, *B*, and *C* (an arbitrary point in the structure) in the system shown in Figure 5.9a is:

$$\begin{bmatrix} \boldsymbol{F_A} \\ \boldsymbol{F_B} \\ \boldsymbol{F_C} \\ \boldsymbol{M_A} \\ \boldsymbol{M_B} \\ \boldsymbol{M_C} \end{bmatrix} = \begin{bmatrix} \boldsymbol{K^T_{AA}} & \cdots & \boldsymbol{K^T_{AC}} & \boldsymbol{K^{TR}_{AA}} & \cdots & \boldsymbol{K^{TR}_{AC}} \\ \vdots & \ddots & \vdots & \vdots & \ddots & \vdots \\ \boldsymbol{K^T_{CA}} & \cdots & \boldsymbol{K^T_{CC}} & \boldsymbol{K^{TR}_{CA}} & \cdots & \boldsymbol{K^{TR}_{CC}} \\ \boldsymbol{K^{RT}_{AA}} & \cdots & \boldsymbol{K^{RT}_{AC}} & \boldsymbol{K^R_{AA}} & \cdots & \boldsymbol{K^R_{AC}} \\ \vdots & \ddots & \vdots & \vdots & \ddots & \vdots \\ \boldsymbol{K^{RT}_{CA}} & \cdots & \boldsymbol{K^{RT}_{CC}} & \boldsymbol{K^R_{CA}} & \cdots & \boldsymbol{K^R_{CC}} \end{bmatrix} \begin{bmatrix} \boldsymbol{D_A} \\ \boldsymbol{D_B} \\ \boldsymbol{D_C} \\ \boldsymbol{R_A} \\ \boldsymbol{R_B} \\ \boldsymbol{R_C} \end{bmatrix} \tag{5.4}$$

where $\boldsymbol{F_{i\ (i=A,B,C)}}$, $\boldsymbol{M_{i\ (i=A,B,C)}}$, $\boldsymbol{D_{i\ (i=A,B,C)}}$, and $\boldsymbol{R_{i\ (i=A,B,C)}}$ are all three dimensional vectors representing forces, bending moments, displacements, and rotations at the corresponding points, respectively (Takahashi 1986). In Equation 2.1 of the original U^* index, only the translational DOFs are considered. Therefore, the internal stiffness tensor $\boldsymbol{K_{ij\ (i=A,B,C;j=A,B,C)}}$ in Equation 2.1 only characterizes the relationship between forces and

displacements. With the introduction of the rotational DOFs, the relationship of the internal stiffness becomes more complicated. In other words, the interaction between the rotational and the translational DOFs should be considered as well. As a consequence, in Equation 5.4, $\boldsymbol{K}^{\boldsymbol{T}}_{\boldsymbol{ij(i=A,B,C;j=A,B,C)}}$, $\boldsymbol{K}^{\boldsymbol{R}}_{\boldsymbol{ij(i=A,B,C;j=A,B,C)}}$, $\boldsymbol{K}^{\boldsymbol{TR}}_{\boldsymbol{ij(i=A,B,C;j=A,B,C)}}$, $\boldsymbol{K}^{\boldsymbol{RT}}_{\boldsymbol{ij(i=A,B,C;j=A,B,C)}}$ are defined as the internal stiffness tensors and they respectively describe the relationships between forces and displacements, moments and rotations, forces and rotations, moments and displacements, respectively.

In Figure 5.9a, since point *B* is fixed ($\boldsymbol{D_B} = \boldsymbol{R_B} = 0$),

$$\boldsymbol{F_A} = \boldsymbol{K^T_{AA}D_A} + \boldsymbol{K^T_{AC}D_C} + \boldsymbol{K^{TR}_{AA}R_A} + \boldsymbol{K^{TR}_{AC}R_C} \tag{5.5}$$

$$\boldsymbol{M_A} = \boldsymbol{K^{RT}_{AA}D_A} + \boldsymbol{K^{RT}_{AC}D_C} + \boldsymbol{K^R_{AA}R_A} + \boldsymbol{K^R_{AC}R_C} \tag{5.6}$$

The external work of the system caused by the force $\boldsymbol{F_A}$ and the bending moment $\boldsymbol{M_A}$ are presented in Equation 5.5 and Equation 5.6, respectively.

$$W_F = \frac{1}{2}\boldsymbol{F_A} \cdot \boldsymbol{D_A} = \frac{1}{2}(\boldsymbol{K^T_{AA}D_A} + \boldsymbol{K^T_{AC}D_C} + \boldsymbol{K^{TR}_{AA}R_A} + \boldsymbol{K^{TR}_{AC}R_C}) \cdot \boldsymbol{D_A} \tag{5.7}$$

$$W_M = \frac{1}{2}\boldsymbol{M_A} \cdot \boldsymbol{R_A} = \frac{1}{2}(\boldsymbol{K^{RT}_{AA}D_A} + \boldsymbol{K^{RT}_{AC}D_C} + \boldsymbol{K^R_{AA}R_A} + \boldsymbol{K^R_{AC}R_C}) \cdot \boldsymbol{R_A} \tag{5.8}$$

Figure 5.9b shows the arbitrary point *C* ($\boldsymbol{D_C} = \boldsymbol{R_C} = 0$) of the system is restrained while same displacements $\boldsymbol{D_A}$ and $\boldsymbol{R_A}$ are applied at point *A*. Equation 5.9 and Equation 5.10 indicate the external work of the modified system induced by the force $\boldsymbol{F'_A}$ and the bending moment $\boldsymbol{M'_A}$, respectively.

$$W_F' = \frac{1}{2}\boldsymbol{F_A'} \cdot \boldsymbol{D_A} = \frac{1}{2}(\boldsymbol{K_{AA}^T D_A} + \boldsymbol{K_{AA}^{TR} R_A}) \cdot \boldsymbol{D_A} \tag{5.9}$$

$$W_M' = \frac{1}{2}\boldsymbol{M_A'} \cdot \boldsymbol{R_A} = \frac{1}{2}(\boldsymbol{K_{AA}^{RT} D_A} + \boldsymbol{K_{AA}^{R} R_A}) \cdot \boldsymbol{R_A} \tag{5.10}$$

The U^*_M index with six DOFs is defined as:

$$U_M^* = 1 - \frac{U_{system}}{U'_{system}} = 1 - \frac{W_F + W_M}{W_F' + W_M'} \tag{5.11}$$

where U_{system} is the total strain energy of the original system (see Figure 5.9a) and U'_{system} is the total strain energy of the modified system (see Figure 5.9b). Here, the total strain energy of the system is transformed from the external work (Beer et al. 2006). Equation 5.11 can be rewritten as:

$$1 - \frac{W_F + W_M}{W_F' + W_M'} = [-\frac{W_F' + W_M'}{(W_F + W_M) - (W_F' + W_M')}]^{-1} \tag{5.12}$$

By minus 1 and then plus 1, Equation 5.12 equals to:

$$\begin{aligned}[-\frac{W_F' + W_M'}{(W_F + W_M) - (W_F' + W_M')} - \frac{(W_F + W_M) - (W_F' + W_M')}{(W_F + W_M) - (W_F' + W_M')} + 1]^{-1} \\ = [1 - \frac{W_F + W_M}{(W_F + W_M) - (W_F' + W_M')}]^{-1}\end{aligned} \tag{5.13}$$

By substituting Equation 5.7~5.10 into Equation 5.13,

$$U_M^* = \left[1 - \frac{2W_F + 2W_M}{(\boldsymbol{K_{AC}^T D_C}) \cdot \boldsymbol{D_A} + (\boldsymbol{K_{AC}^{TR} R_C}) \cdot \boldsymbol{D_A} + (\boldsymbol{K_{AC}^{RT} D_C}) \cdot \boldsymbol{R_A} + (\boldsymbol{K_{AC}^{R} R_C}) \cdot \boldsymbol{R_A}}\right]^{-1} \tag{5.14}$$

It can be seen from Equation 5.14 that the U^*_M index is only related to the internal stiffness between the loading point and the arbitrary point of the system. Hence, the U^*_M index is applicable for identifying the load paths of six DOFs systems.

5.2.2 Case study of the U^*_M index

The proposed U^*_M index and the original U^* index were derived based on the same theoretical foundation. The original U^* index can be applied to 3-D continuum models, while the proposed U^*_M index is valid for systems under six DOFs (e.g. plate or shell models). For the same structure, although the selected mechanical models are different, the proposed U^*_M index and the original U^* index shall provide similar results. In the following case study, both of the proposed U^*_M index and the original U^* index were calculated for the same sample structure, i.e. a steel plate with the length of 250 mm, the width of 150 mm, and the thickness of 10 mm as shown in Figure 5.10. The plate is subjected to transverse shear forces in Z-direction (out of the plane). In the computation of the U^*_M index, shell elements were used for modeling the plate, whereas the sample structure was simulated by solid elements when calculating the original U^* index.

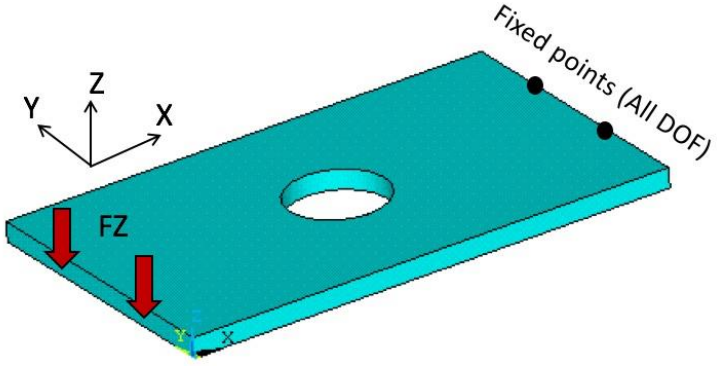

Figure 5.10: The sample structure for U^* and U^*_M computations.

In the U^* index theory, U^*_1 is the index of the transmission of the applied forces, U^*_2 is the index of the transmission of the reaction forces of the system, and U^*_{sum} is the summation of U^*_1 and U^*_2. The distributions of U^*_1, U^*_2, and U^*_{sum} indices are important because the load paths and the U^* based design criteria are generated according to them as introduced in Chapter 2. As a result, the current case study focuses on the comparisons of all these three indices. Figure 5.11a and Figure 5.11b show the comparison of the U^*_{M1} and the U^*_1 distributions of the sample structure illustrated in Figure 5.10, the distributions of the U^*_{M2} and the U^*_2 are compared by Figure 5.12a and Figure 5.12b, while Figure 5.13a and Figure 5.13b respectively elaborate the U^*_{sum} distributions of the shell model and the solid model. The results of the comparisons indicate the U^*_M distribution of the shell model has a good consistency with the U^* distribution of the solid model.

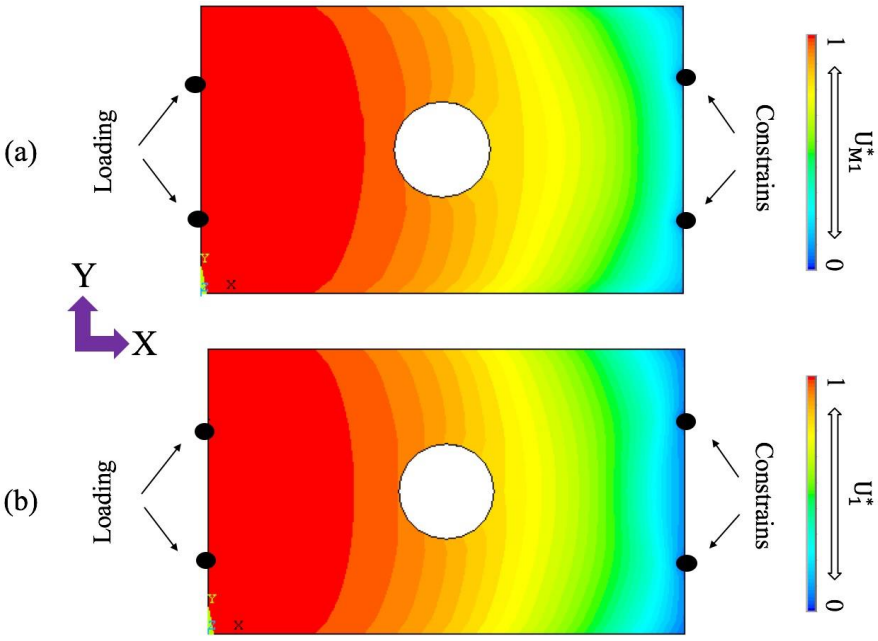

Figure 5.11: Results based on the applied forces- a): The U^*_{M1} distribution of the shell model; b): The U^*_1 distribution of the solid model.

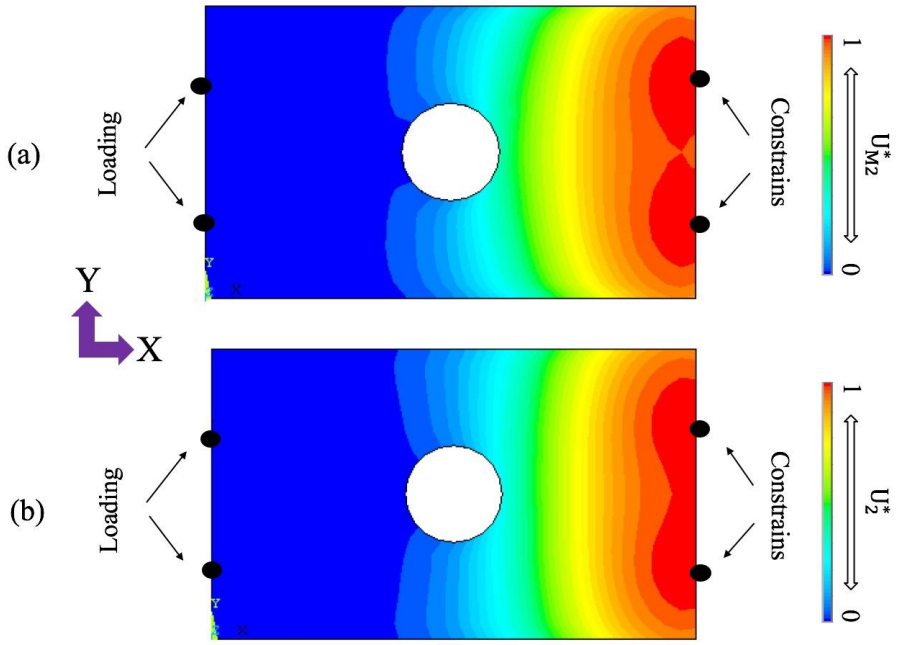

Figure 5.12: Results based on the reaction forces- a): The U^*_{M2} distribution of the shell model; b): The U^*_2 distribution of the solid model.

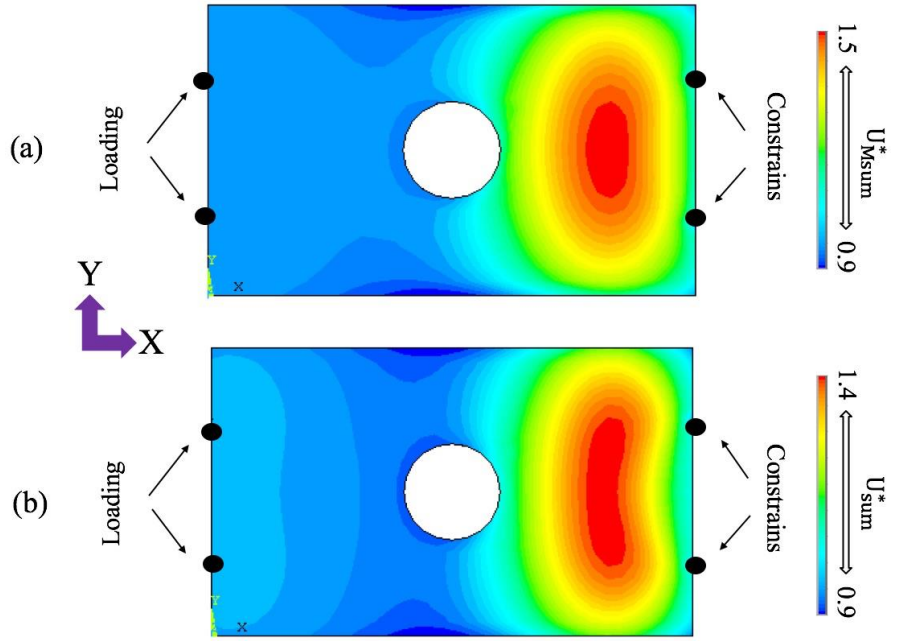

Figure 5.13: Distributions of the U^*_{sum} index of- a): The shell model (U^*_{Msum}); b): The solid model (U^*_{sum}).

5.3 Summary

In this chapter, two new load transfer indices (U^*_O and U^*_M) have been successfully proposed to extend the scope of the application of the U^* index theory in structural analysis. Compared to the original U^* index, the new U^*_O index is the more universal form for both orthotropic and isotropic materials. The U^*_O index has been demonstrated to be sensitive with the fiber directions of the composite structure and it can give reasonable load paths for orthotropic composite structures. Composite materials are used instead of conventional metals to improve the structural weight-efficiency. As introduced in Chapter 1 that an appropriate enhancement along the main load paths of the composite structure can further increase the structural weight-efficiency. This can be accomplished based on the load transfer analysis using the U^*_O index.

In addition, the U^* theory has been developed as a design paradigm for designing structures with high efficiency and performance. However, an inaccurate U^* analysis may induce improper design modifications and thus degrades the integrity of the structure. To obtain more precise load paths, the orthotropic material property is recommended rather than the isotropy when the load transfer analysis is conducted for composite materials.

The U^* index can visualize load paths for engineering structures providing designers with valuable information in addition to the conventional stress analysis. However, by initially neglecting of the rotational DOFs, the original U^* index is incompatible with shell elements which are essential in finite element analysis of thin-walled structures. To overcome this limitation, this chapter successfully introduced a new U^*_M index by considering both translational and rotational DOFs. The results provided by the proposed

U^*_M index are consistent with the original U^* index which has been validated through two separate experiments. The new U^*_M index bridged the gap between the U^* index theory and the plate and shell theory and thus makes the U^* index theory more powerful and efficient for load transfer analysis of thin-walled structures.

Chapter 6

Application of the U^*_M Index in Structural Analysis and Modification

In this chapter, an application of the newly proposed U^*_M index is presented to show its effectiveness and significance in engineering structural design analysis. In FEA, each node of a shell element has three translational DOFs and three rotational DOFs. Therefore, the original U^* index which only considers translation DOFs is invalid for calculating the load path of the finite element (FE) model built by shell elements. However, as a valuable alternative to solid elements, shell elements are preferred for thin-walled structures since they are more efficient in both modeling and computation. For example, in a parametric study of the structural thickness, the FE model based on solid elements has to be rebuilt due to the variation of the thickness. However, the remodeling is not needed when shell elements are utilized.

The proposed U^*_M index benefits engineers with the advantages of reduced complexity of shell elements over solid elements. However, the comparison between shell and solid elements is not the focus of the current study. The main purpose of the application in this chapter is to show effectiveness and significance of the newly proposed U^*_M index in

engineering structural design and analysis. The capability of the original U^* index has already been demonstrated by researchers and engineers. Hence, this Chapter puts the emphasis on the computational analysis where only the new U^*_M index is applicable while the original U^* index is not. Accordingly, in this case study, a complex thin-walled structure is chosen as the sample structure where shell elements are preferred for the finite element modeling than solid elements. Thus, the proposed U^*_M index is applied instead of the original U^* index in the structural analysis and the design modification.

6.1 Load transfer analysis

The sample structure of the case study is a parcel rack strut in a bus as shown in Figure 6.1a. The strut is a thin-walled structure with the length of 640 mm, the height of 320 mm, the width of 73 mm, and the thickness from 2.9 mm to 7.0 mm. The material properties of the strut are presented in Table 6.1. Figure 6.1b shows the computational model of the strut, where vertical forces towards the floor of the bus are applied at the aisle handrail mount to simulate the working load of the strut, while the outside and the aisle ceiling mounts of the strut are fully constrained. The computational model of the strut was developed using the commercial finite element code ANSYS 15.0 (ANSYS 2014). The finite element model of the strut (see Figure 6.1b) consists of 2,651 four-node shell 181 elements. This type of shell element is suitable for analyzing thin to moderately thick structures (ANSYS 2013). Full integration with incompatible modes (KEYOPT(3)=2) is considered in the formulation of the shell element to ensure a high accuracy even with a coarse mesh (Simo and Armero 1992).

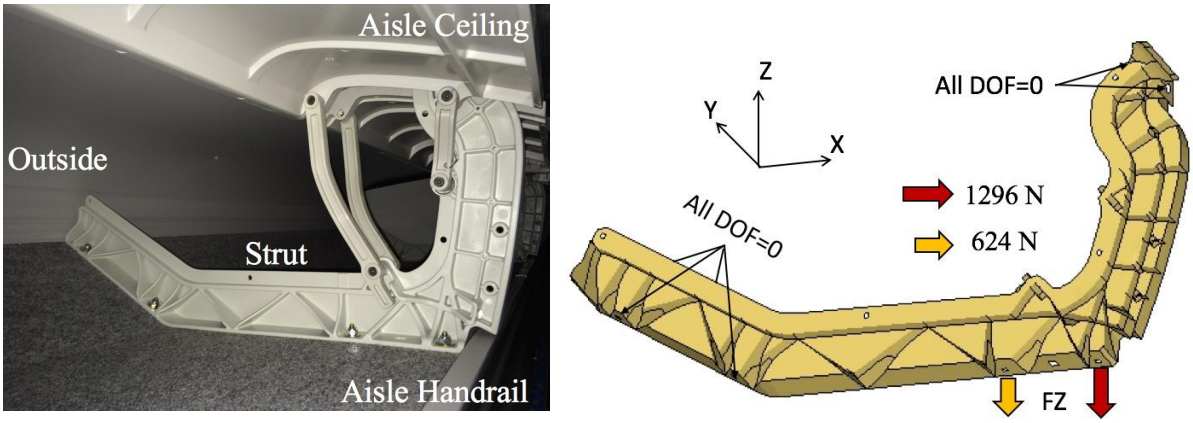

(a) (b)

Figure 6.1: Sample structure of the case study- a): The parcel rack strut; b): Computational model of the strut.

Table 6.1: Material properties of the strut (Chen et al. 2008).

Component	Material	Density (kg/m^3)	Modulus (GPa)	Poisson's ratio
Strut	Nylon	1.15	1.9	0.4

The U^*_M index can predict reasonable load paths without being affected by the phenomenon of stress concentration. Figure 6.2a depicts the U^*_M distribution and the resultant main load paths (red arrows) of the parcel rack strut. The U^*_M analysis shows the main portion of the load is carried by the rib stiffeners. Figure 6.2b shows the von Mises stress distribution of the structure and three marked locations with peak stresses. However, such load paths as presented in Figure 6.2a cannot be obtained based on the stress distribution shown in Figure 6.2b because the rib stiffeners are subjected to the lower stresses.

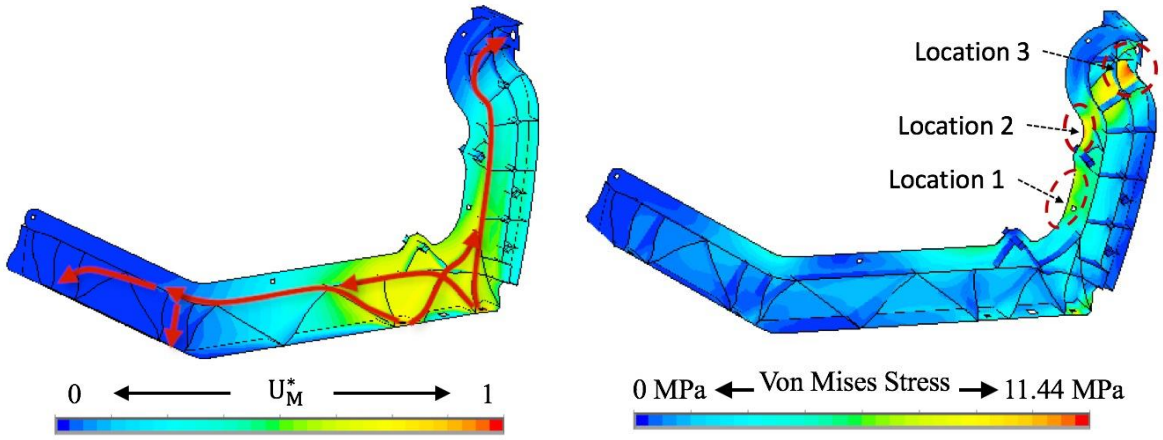

(a) (b)

Figure 6.2: Computational results of the strut- a): U^*_M distribution and the main load paths (red arrows); b): Distribution of von Mises stress.

Figure 6.3a illustrates the U^*_M variation along a specific path (solid black arrow) pointing from the loading points to the supporting points in the vertical part of the strut. Same pattern can be seen in Figure 6.3b for the horizontal part of the strut. In a load bearing structure, the U^*_M value decreases from 1 at the loading point to 0 at the supporting point. The decay of the U^*_M index in a structure with perfect stiffness distribution should be uniform. In other words, sudden changes of the U^*_M index means the stiffness distribution of the structure is unreasonable (Sakurai et al. 2003).

As shown in Figure 6.3a, the U^*_M index at Location 1 drops sharply and then goes up fast. This indicates the stiffness in that location is significantly lower than the adjacent areas. In other words, that location cannot resist the applied forces as well as the adjacent areas. Hence, with the increase of the applied force, the marked area would deform excessively and might cause the failure of the structure. This assumption fully agrees with the result of the quasi-static force testing of the strut, which was conducted along with the

industrial partner as shown in Figure 6.4. Another sudden decrease of the U^*_M index happened at Location 3, which is also one of the locations under the higher stresses (see Figure 6.2b).

In contrast to the vertical part, the U^*_M variation of the horizontal part of the strut is more uniform as shown in Figure 6.3b. Therefore, the horizontal part of the strut has the lower stresses under the working load and the better structural integrity during the quasi-static testing. The above results reveal that the structural failure can be predicted by the stress analysis whereas the U^*_M index can give insights of the structural issues which are important for improving the structural performance.

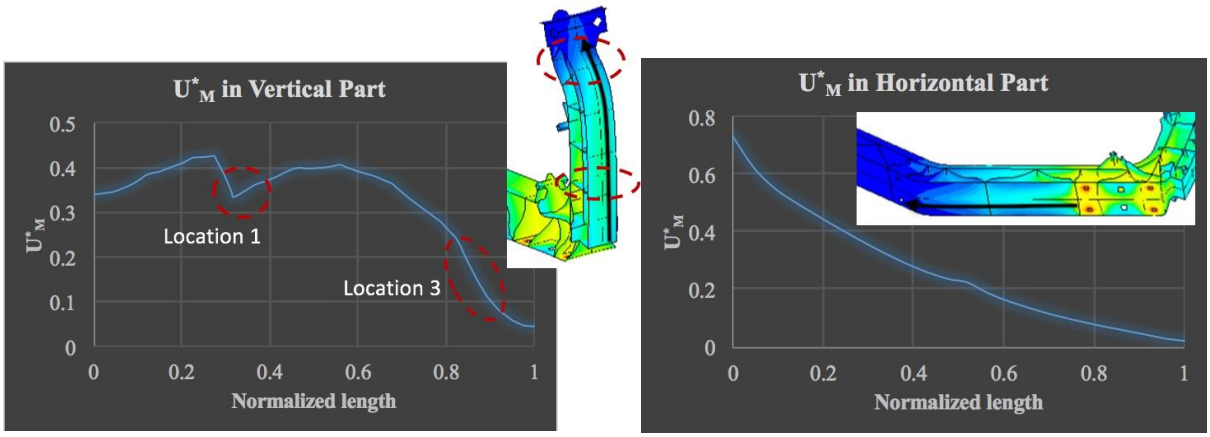

(a) (b)

Figure 6.3: U^*_M variation along a specific path in- a): Vertical part of the strut; b): Horizontal part of the strut.

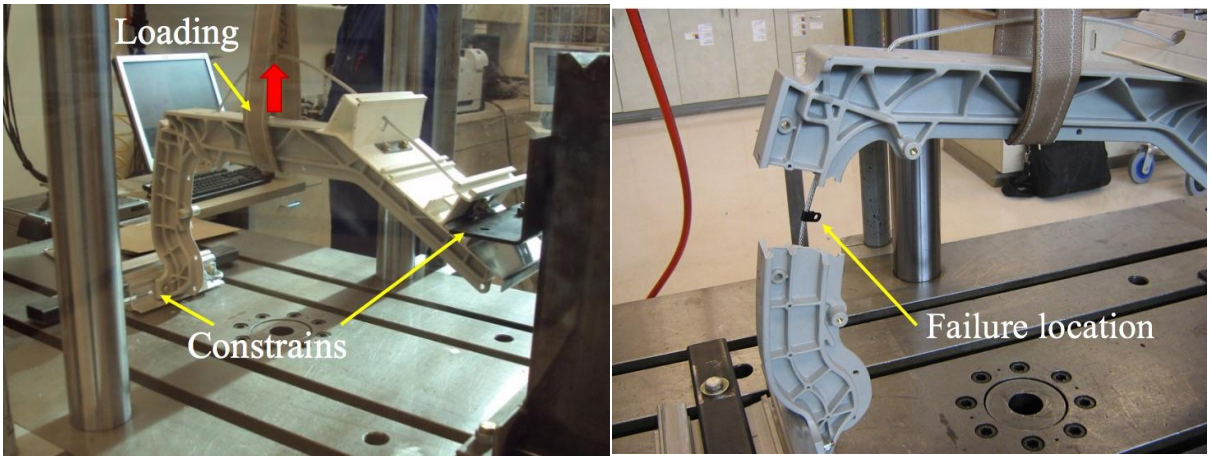

(a) (b)

Figure 6.4: Quasi-static force testing of the parcel rack strut- a): Testing setup; b): The failure location.

6.2 Design modification

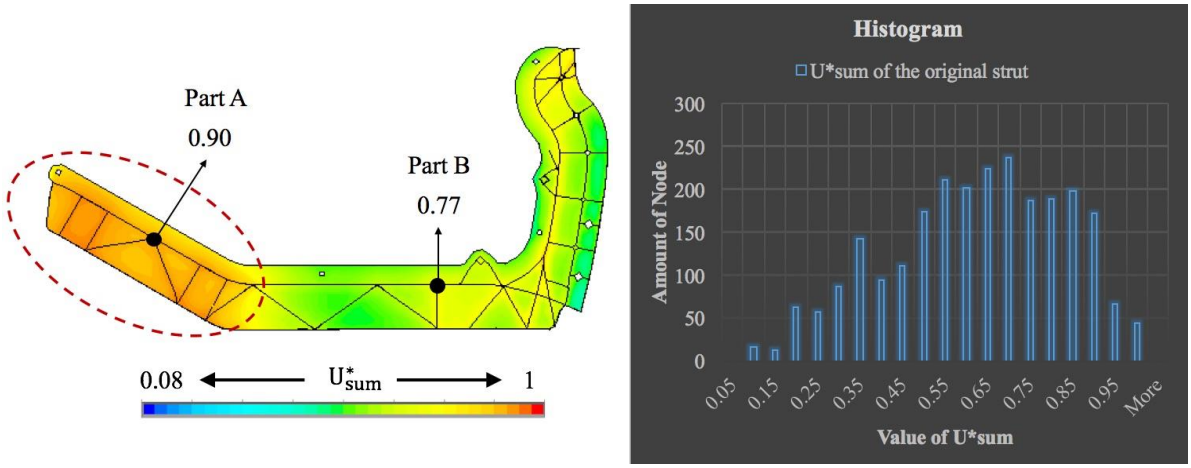

(a) (b)

Figure 6.5: The U^*_{sum} index of the original strut- a): U^*_{sum} distribution; b): U^*_{sum} histogram.

The design modification aims at improving the weight-efficiency of the structure. To be more specific, through the design modification, the mass of the structure is kept as constant while the maximum displacement of the structure is significantly decreased under the same working load demonstrated in Figure 6.1b. As introduced in Chapter 2.3, the rising of the homogeneity of the U^*_{sum} distribution can lead to the increase of the structural weight-efficiency. As a result, the homogeneity of the U^*_{sum} index is used as the design criterion for the design modification.

The U^*_{sum} distribution in the parcel rack strut was calculated as shown in Figure 6.5a. To simplify the design process, the sample structure was considered to be only comprised of two parts. Based on the U^*_{sum} distribution, the marked area in Figure 6.5a is defined as part *A* while the rest of the strut is defined as part *B*. The U^*_{sum} values of two marked points in Figure 6.5a are used as the representative U^*_{sum} values for part *A* and part *B*, respectively.

It can be seen from Figure 6.5a that the U^*_{sum} value of part *A* is remarkably higher that part *B*. The design modification focused on harmonizing the U^*_{sum} values between those two parts. To do so, firstly, the thickness of each element of part *A* was reduced by following Equation 6.1.

$$t_R = t_0(1 - pN) \tag{6.1}$$

In Equation 6.1, t_R is the reduced thickness, t_0 is the original thickness, p is percentage of the thickness reduction in each step, N is the number of the modification step. In this study, p is set as 2%, thus the maximum value of N is 50. To keep a consistent mass during the

design modification, in each step, the removed material was added back to the full structure. The new thickness of the strut can be obtained through Equation 6.2:

$$t_N = t_R \frac{M}{m} \tag{6.2}$$

where t_N is the new thickness of each part of the strut, M is the mass of the original strut and m is the mass of the strut after the material reduction. After each modification step, the U^*_{sum} values of part *A* and part *B* were computed again to see if they are equal or not. If not, the design modification would continue with $N=N+1$. As can be seen in Figure 6.6, the U^*_{sum} values of part *A* and part *B* become consistent with each other in the 29th step. Then, the desirable thickness of the elements in part *A* can be calculated through Equations 6.1 and 6.2 when N equals to 29.

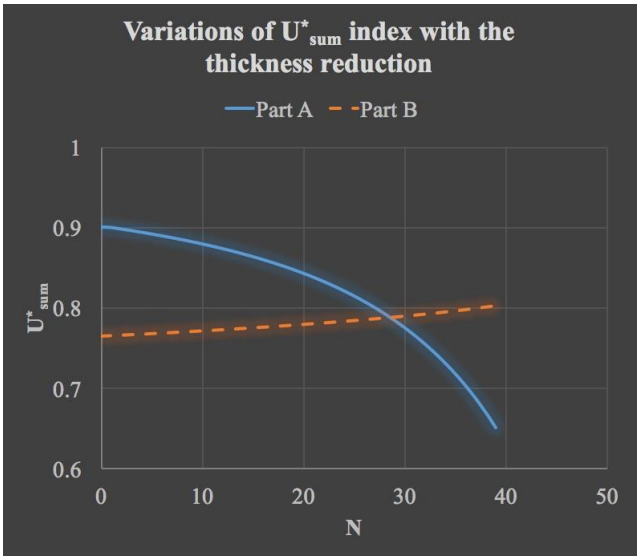

Figure 6.6: The variation of the U^*_{sum} index in each step of the thickness reduction.

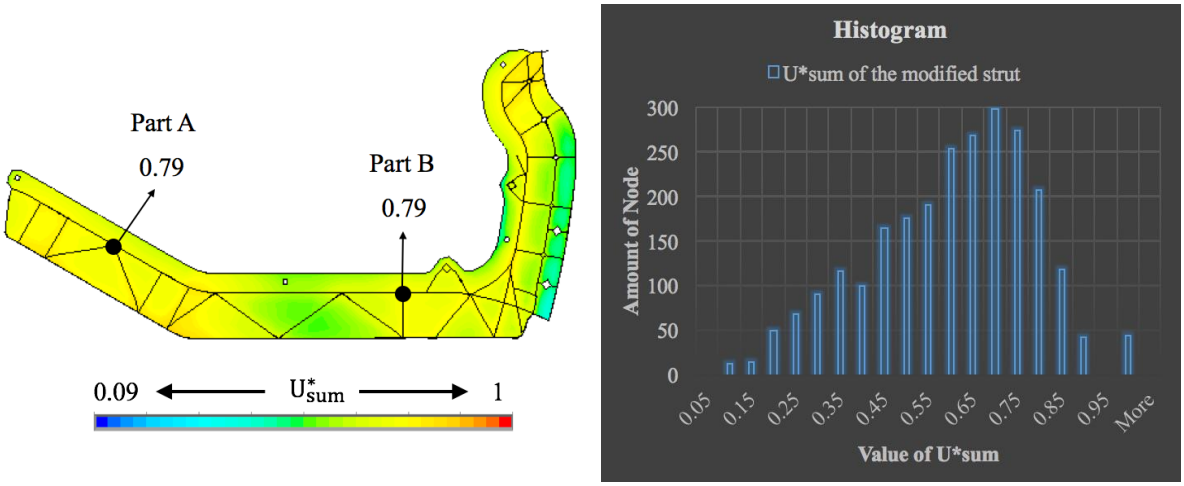

(a) (b)

Figure 6.7: The U^*_{sum} index of the modified strut- a): U^*_{sum} distribution; b): U^*_{sum} histogram.

Figure 6.7a presents the U^*_{sum} distribution of the modified strut. It can be seen from Figure 6.7a and Figure 6.5a, the modified strut has the higher homogeneity of the U^*_{sum} index than the original one. Same conclusion can be drawn when comparing the histograms of the U^*_{sum} values of the modified (see Figure 6.7b) and the original (see Figure 6.5b) struts.

The structural parameters of both the original and the modified struts are presented in Table 6.2. The displacements and the stresses of both structures were calculated based on the same loading conditions as shown in Figure 6.1b. Figure 6.8a and Figure 6.8b depict the contour plots of the total displacements of the original and the modified structures, respectively.

Table 6.2: Structural parameters of both original and modified struts

Model	Mass (Kg)	Maximum displacement (mm)	Maximum von Mises stress (MPa)
Original Strut	1.27	0.97	11.44
Modified Strut	1.27	0.82	9.22

The stiffness to mass ratios of the original strut (c_0) and the modified strut (c_1) are defined by Equation 6.3 and Equation 6.4, where M is the mass, k_0 and k_1 are the overall stiffness of the original and the modified struts, respectively. The overall stiffness of the original and the modified struts can be calculated through Equation 6.5 and Equation 6.6 based on the same external force (f) demonstrated in Figure 6.1b. d_0 (in Equation 6.5) and d_1 (in Equation 6.6) are the maximum displacements of the original and the modified struts, respectively.

$$c_0 = \frac{k_0}{M} \tag{6.3}$$

$$c_1 = \frac{k_1}{M} \tag{6.4}$$

$$k_0 = \frac{f}{d_0} \tag{6.5}$$

$$k_1 = \frac{f}{d_1} \tag{6.6}$$

By substituting Equation 6.5 and Equation 6.6 into Equation 6.3 and Equation 6.4, the improvement of the structure in terms of the stiffness to mass ratio can be calculated as:

$$\frac{c_1 - c_0}{c_0} = \frac{c_1}{c_0} - 1 = \frac{d_0}{d_1} - 1 = 18.3\% \tag{6.7}$$

It can be seen from Equation 6.7 that the stiffness to mass ratio of the strut is improved by 18.3% through the design modification using the new U^*_M index. The presented process of the design modification is similar to the stress or strain energy based sizing optimization methods introduced in (Christensen and Klarbring 2009; Li et al. 2015).

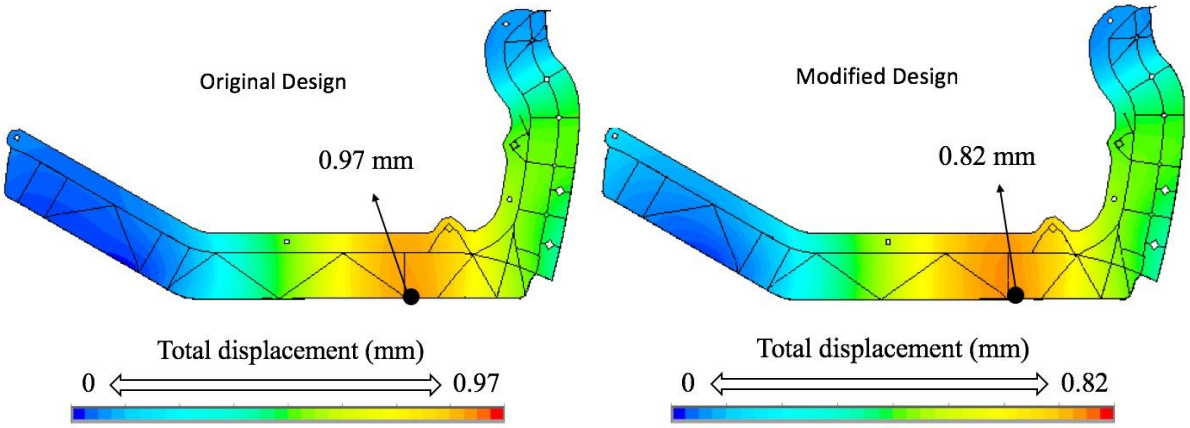

Figure 6.8: Total displacements of- a): The original strut; b): The modified strut.

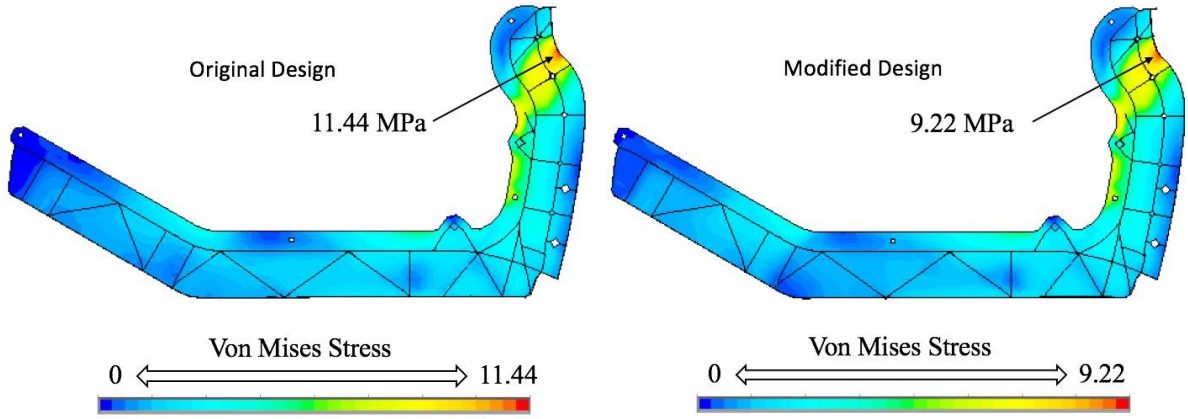

(a) (b)

Figure 6.9: Von Mises stress distributions of- a): The original strut; b): The modified strut.

6.3 Summary

In this chapter, structural analysis and modification was successfully conducted to a complex thin-walled structure based on the utilization of the U^*_M index. The results demonstrate that the load transfer analysis based on the U^*_M index is an effective tool for structural evaluation and design improvement. Being used in conjunction with the conventional finite element analysis, the U^*_M analysis can provide designers with supplementary information which are valuable for decision making.

The presented load paths analysis indicates that the U^*_M index can predict accurate load paths for complex thin-walled structures which are modeled by shell elements. Moreover, the U^*_M analysis can provide designers with the insight of the structural issues and the directions of the structural modifications, which cannot be obtained directly from the distributions of stresses and displacements.

The proposed design modification demonstrates that the homogeneity of the U^*_{sum} index can be applied as a design criterion for evaluating the structural weight-efficiency. The improvement of the homogeneity of the U^*_{sum} index can result in the increase of the structural weight-efficiency such as stiffness to weight ratio. Decreasing the materials from the parts with higher U^*_{sum} values is an effective way to raise the homogeneity of the U^*_{sum} index.

The weight-efficiency of the sample structure was considerably improved through the design modification based on the U^*_M and the U^*_{sum} indices. The approach applied in the redesign process has great potential to be further developed as a formal size optimization method for engineering structures, which is set as the future work of the thesis.

Chapter 7

Load Transfer Analysis of a Bus Bay Section for Rollover Protection Using the U^*_M Index

In this chapter, an application of the newly proposed U^*_M index on load transfer analysis of bus rollover is presented. The bus structure is basically comprised of thin-walled tubes and plates. The FE model of the bus bay section is established using shell elements. Therefore, the original U^* index is not capable for computing the load path of the bus model. The approach proposed in the current chapter has been effectively applied to the industrial project which aimed at improving the performance of the bus structure during rollover collisions.

7.1 Introduction of bus rollover protection

Regulation ECE R66

Bus rollover often induces severe injuries and even fatalities (see Figure 7.1). As a result, United Nation Economic Commission of Europe enacted Regulation No. 66 (ECE R66) to ensure a survival space of buses for protecting occupants both during and after the rollover test (UNECE 2006). “Survival space” means a space to be reserved in the

passengers', crew and driver's compartments to provide them with better survival possibility in case of a rollover accident.

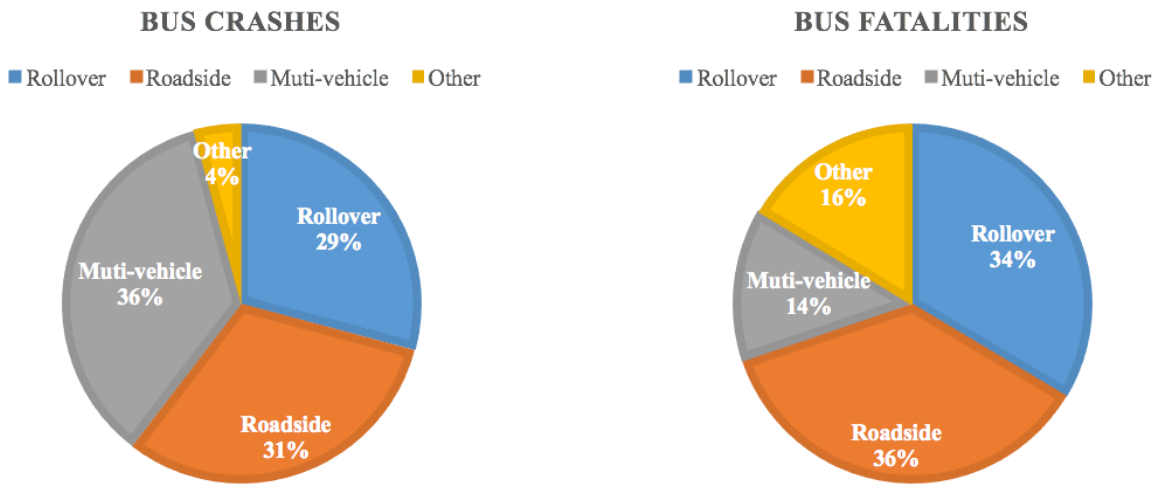

Figure 7.1: Bus crashes and fatalities based on the most harmful events (FARS 1996-2005)

The rollover test is a lateral tilting test as shown in Figure 7.2a. During the rollover test, the vehicle is tilted slowly on the tilting platform until it reaches the unstable equilibrium position. Then, the vehicle starts to rollover with a zero angular velocity and the rotation axis going through the wheel-ground contact points. The rollover test should be conducted in a ditch having smooth, dry, and horizontal concrete ground surface with a nominal depth of 800 mm. The superstructure of the vehicle should have sufficient resistance to keep the survival space in perfect condition during and after the rollover test. "Perfect Condition" means no structural part which is outside the survival space before the test intrudes into the survival space, meanwhile no part of the survival space projects outside the deformed structure (UNECE 2006). The envelope of the survival space for the vehicle is defined by

building vertical transverse plane inside the vehicle with the periphery as depicted in Figure 7.2b.

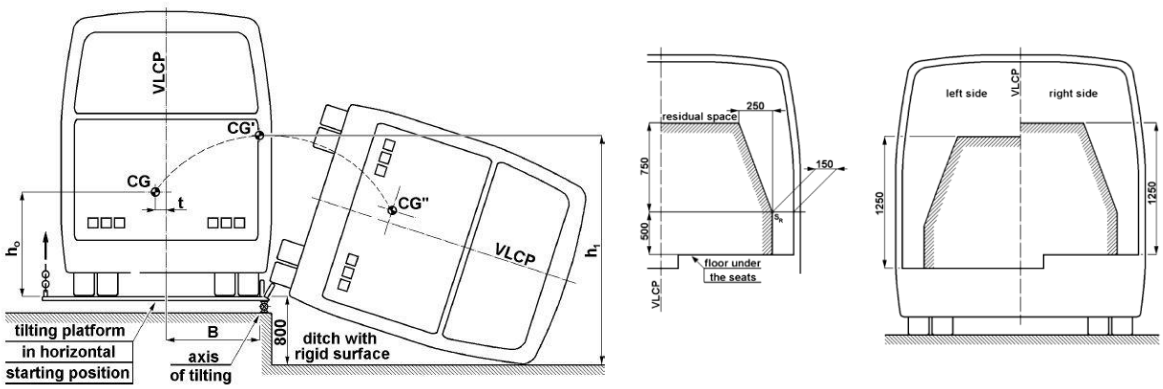

(a) (b)

Figure 7.2: Specification of the rollover test in ECE R66 (UNECE 2006)- a): Bus rollover test, b): Illustration of the survival space.

Bus Bay Section

The bus superstructure is the load bearing components of the bus body containing those coherent parts and elements which contribute to the strength and energy absorbing capability of the bus body, and preserve the survival space in the rollover test. A bus bay is a structural section of the superstructure forming a closed loop between two planes which are perpendicular to the vertical longitudinal central plane of the vehicle. A bay contains one window (or door) pillar on each side of the vehicle as well as side wall elements, a section of the roof structure and a section of the floor and underfloor structure.

Compared to the whole bus superstructure, a bus bay section is more efficient in modeling, computation, and modification. As a result, bus bay sections are widely used by engineers for studying the bus structural performance under rollover impact (Li et al. 2012;

Roca et al. 1997). In the current chapter, a bus bay section is extracted from the full bus model for investigating the load transfer behavior of the bus superstructure during the rollover collision.

Motivation and Objective

To keep any part from intruding into the survival space due to large local deformations, the impact force should be transferred properly and uniformly within the bus superstructure during the rollover test. Consequently, the load transfer analysis of bus superstructure under the rollover impact is very imperative.

With the development of simulation technology, computer simulation has been increasingly used to study bus rollover performance instead of physical test which is costly in both time and money. During the past two decades, many computational models have arisen for bus rollover analysis using finite element analysis (FEA) (Friedman et al. 2015; Guler et al. 2007; Li et al. 2012; Liang and Le 2010; Liang and Le 2009; Roca et al. 1997). However, the existing studies of the bus rollover as introduced above are mainly focused on stresses and strains of the bus structure. A load transfer analysis of the bus structure by considering the rollover collision remains limited to date.

Hence, the objective of the work presented in this chapter is to establish an approach for conducting load transfer analysis of the bus superstructure for rollover protection under the legislated regulation ECE R66.

7.2 Computational methods

7.2.1 Rollover simulation using LS-DYNA

The rollover simulation of the bus structure in the current study is based on the test procedure defined in regulation ECE R66 as introduced in Section 7.1. The FE model of the bus bay section was extracted from a full bus model as shown in Figure 7.3. The bus bay section is 1989.64mm in length, 2445.44mm in width, 3219.09mm in height and 1807kg in weight. It includes the roof, the side walls, the seats, the floor and the underfloor structure, which corresponds to the requirement of the regulation ECE R66. The rollover simulation of the structure is performed using explicit finite element code LS-DYNA (LSTC 2015). All the deformable parts of the bus bay section are modelled by four nodes Belytschko-Tsay shell elements with reduced integration. This type of shell element has a good combination of both computational efficiency and accuracy (Liang and Le 2009). The FE model of the bay section consists of approximately 187,000 shell elements and 65 mass points.

The elastic-plastic material model *MAT_024, *MAT_PIECEWISE_LINEAR_ PLASTICITY is used for deformable parts of the structure. The rigid parts consisting of the tilting platform and the connections between seats and the floor are modelled using *MAT _020, *RIGID_MATERIAL. The material model of the survival space is set as *NULL_ MATERIAL for visualisation only. All parts of the bus bay section are included in the single global contact *CONTACT_AUTOMATIC_SINGLE_SURFACE except the seats. This type of contact is suitable for self-contacting problems or large deformation problems where the contact behaviour is hard to estimate beforehand. The contact relationship

between the seats and other parts of the bus is defined as *CONTACT_AUTOMATIC _SURFAC_TO_SURFACE. This type of contact is also used between the bay section and the tilting platform. *CONTACT_TIED_SURFAC_TO_SURFACE is used to constrain the welds and the structure. The contact between the structure and the ground is implemented using *CONTACT_RIGID_WALL_PLANAR.

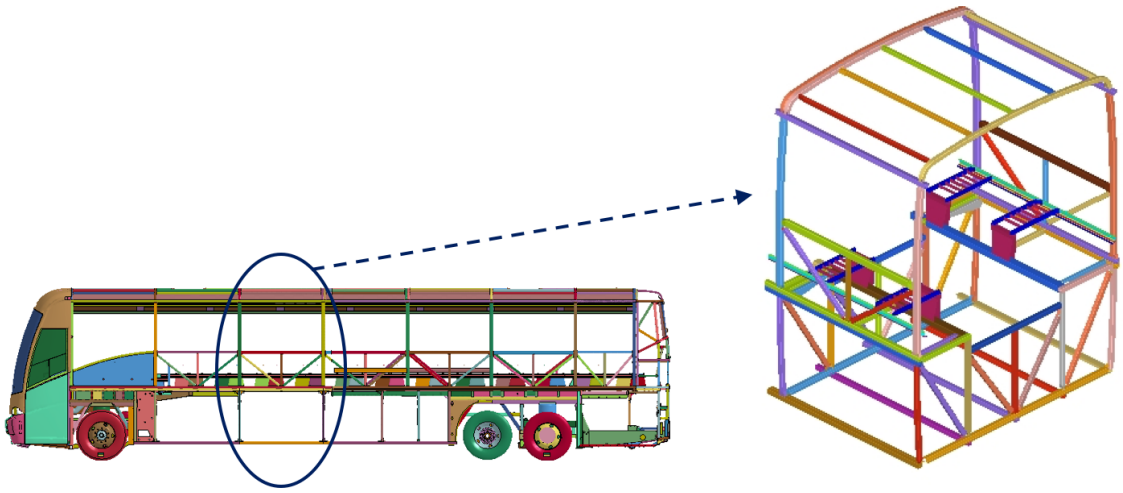

Figure 7.3: Computational model of the bus bay section.

The rollover simulation starts from the unstable equilibrium position of the bus bay section on the tilting platform. The initial rotation velocity is set with a negligible value using the card *INITIAL_VELOCITY_GENERATION. The gravity of the structure is defined as the external loading using the card *LOAD_BODY. To verify the simulation technique, model validation was conducted for a subcomponent of the bus bay section. As shown in Figure 7.4a, the cross window pillars, which are the main elements of the bus bay section, were tested until failure occurred under a quasi-static force. Figure 7.4b illustrates the finite element model of the window cross pillars in LS-DYNA, which is used to simulate the physical testing. A good consistency can be observed between the force-

displacement curves obtained from the physical testing and the LS-DYNA simulation which can be seen in Figure 7.5.

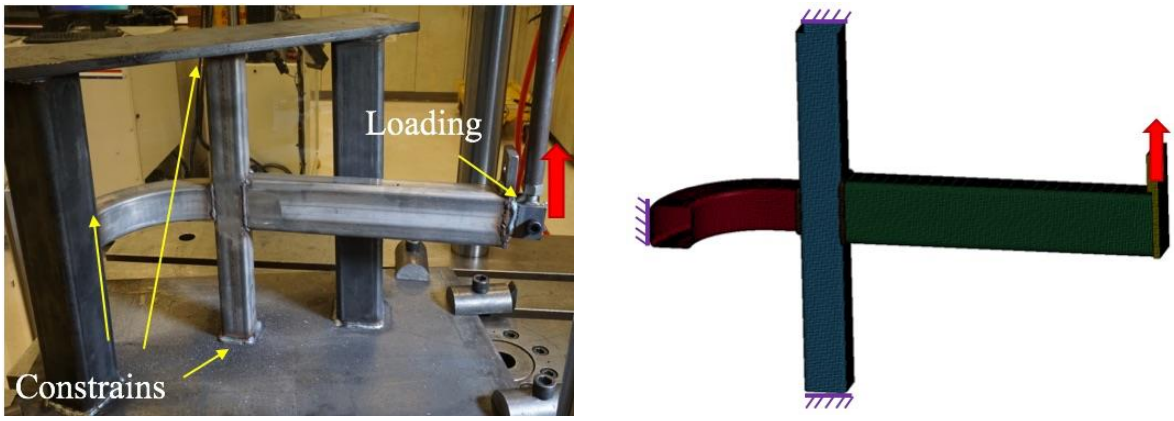

(a) (b)

Figure 7.4: Model validation of window cross pillars- a): Setup of the quasi-static testing; b): Simulation model in LS-DYNA.

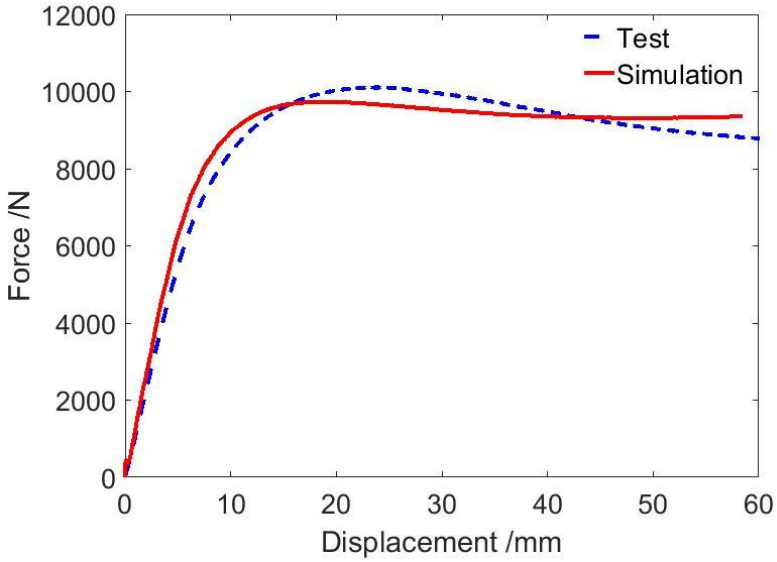

Figure 7.5: Comparison of the force-displacement curves between the simulation and the test.

7.2.2 Equivalent static loading for load transfer analysis

The calculation of the load paths for the whole impact process is costly and unnecessary. As a result, in load transfer analysis of vehicle frontal and side collisions, equivalent static loading conditions were commonly utilized as the representatives of the impact forces (Akima et al. 2015; Wang et al. 2010). In the current study, an equivalent static load is used for the load transfer analysis of the bus bay section.

In ECE R66, a quasi-static loading test of body sections can be used as an equivalent approval method (LSTC 2015). In this equivalent test, the load should be applied gradually until the survival space is invaded by one of the elements of the body section. The bus body section passes the test if the absorbed energy by the body section is not less than the minimum requirement. The application of the quasi-static load to the body section is shown in Figure 7.6a. The direction of the applied load shall be related to the longitudinal vertical center plane of the vehicle and its incline (α) shall be determined by:

$$\alpha = 90° - arcsin\left(\frac{800}{H_C}\right) \tag{7.1}$$

where H_C is the cantrail height (mm) of the vehicle measured from the horizontal plane on which it is standing.

In light of the quasi-static loading test, an equivalent static loading condition of the rollover impact was proposed to the bus bay section as depicted in Figure 7.6b. The direction of the equivalent static load was calculated by Equation 7.1 and the whole bottom of the bay section is fully constrained (see Figure 7.6b).

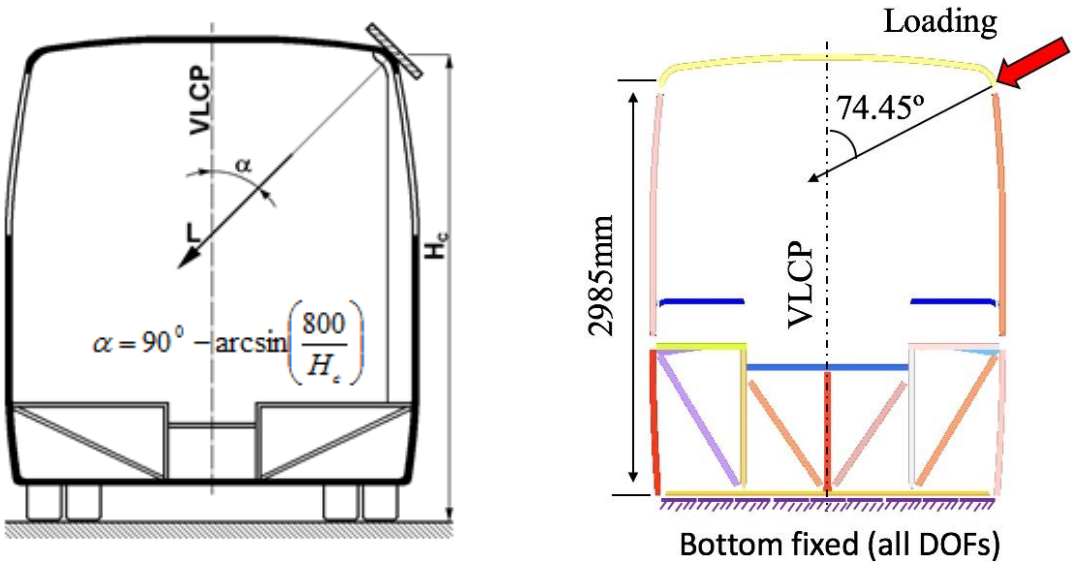

(a) (b)

Figure 7.6: Equivalent static loading conditions of rollover impact.- a): Application of the quasi-static load required by ECE R66 (UNECE 2006); b): Proposed equivalent static loading to the bus bay section.

7.2.3 Load paths calculation

The U^* index theory defines the main load path as the line with the smallest $\boldsymbol{g}^{(-)}$ (stiffness decay vector) in Equation 2.10. Normally, the line with the smallest $\boldsymbol{g}^{(-)}$ is the ridge line of the U^* distributions which was used to determine the load path in the structures presented in the previous chapters. However, such a ridge line is not visible for the bus bay section in the current chapter because it is a truss-like structure. For example, at a cross point of multiple pillars, the main load path shall be determined by comparing the stiffness decay vectors of the pillars.

The following example can interpret how to apply the stiffness decay vector $\boldsymbol{g}^{(-)}$ to determine the main load path at a cross point of multiple pillars. Figure 7.7a shows three

pillars with the same dimensions and material properties connected at point *A*. The other sides of the pillars are fully fixed. The applied force at point *A* and the reaction forces at points *B*, *C*, and *D* are also presented in Figure 7.7a. Figure 7.7b shows the U^*_M variations in the pillars and the associated tangent lines at point *A*. The magnitude of $\boldsymbol{g}^{(-)}$ equals to the slope of the tangent line of the U^*_M curve. As can be seen from Figure 7.7b, the slope of the tangent line of pillar-1 is smaller than that of pillar-2 or pillar-3. In other words, pillar-1 has the smallest $\boldsymbol{g}^{(-)}$ compared to pillar-2 and pillar-3. Therefore, higher force shall be transferred to pillar-1 rather than pillar-2 and pillar-3. The above result can be proved by comparing the reaction forces at the supporting points of the pillars. As shown in Figure 7.7a, point *B* has the higher reaction force compared to point *C* and point *D*.

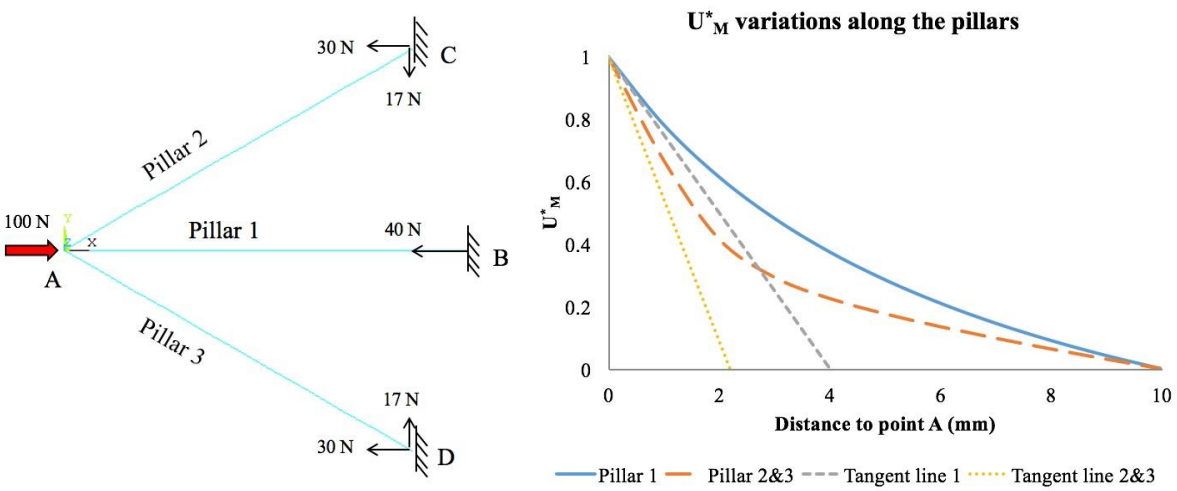

(a) (b)

Figure 7.7: Load paths analysis of the system of cross pillars- a): The applied and the reaction forces of the system; b): U^*_M variations along the pillars.

It has to be pointed out that the above example aimed at proposing an approach for determining the main load path of bus superstructures rather than truss structures in civil

engineering. The truss structures in civil engineering are normally simulated by beam elements. As a result, the above method is not necessary. Nevertheless, a bus structure is much more complicated than a truss. In order to obtain accurate structural response, the finite element model of the bus bay section in the current study is built by shell elements and the proposed approach is therefore needed.

7.3 Results

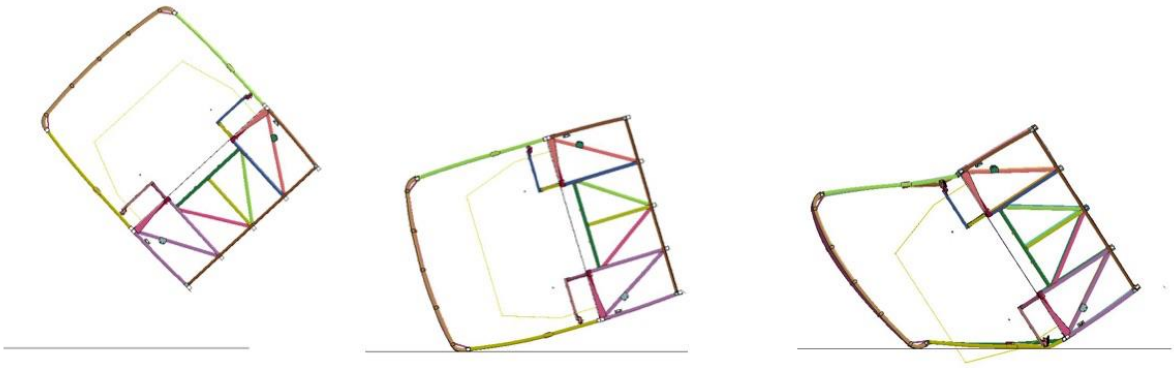

(a) (b) (c)

Figure 7.8: Simulation process of the rollover collision of the bus bay section- a): Unstable equilibrium position; b): First contact with the ground; c): Moment of the maximum deformation.

Figure 7.8a, Figure 7.8b, and Figure 7.8c show the process of the rollover simulation of the bus bay section from LS-DYNA. The energy conservation during rollover simulation can be checked in Figure 7.9. It can be seen from Figure 7.9 that the total energy is constant during the whole simulation process, which is an important indication to a correct result (Friedman et al. 2015; Guler et al. 2007). Meanwhile, it can be observed that the kinetic energy of the bay section is principally converted into the internal energy (strain energy) and the hourglass energy remains negligible.

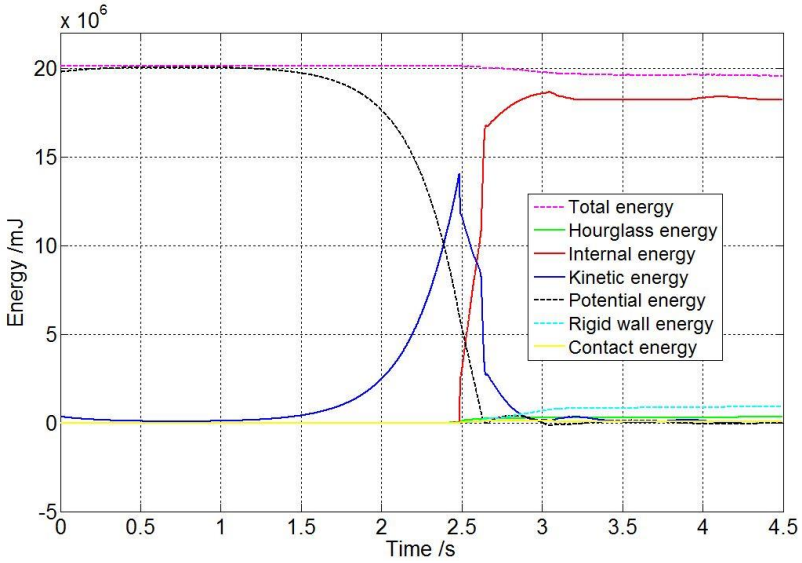

Figure 7.9: Energy conservation during the rollover simulation in LS-DYNA.

The maximum deformation of the bay section during the rollover is presented in Figure 7.10a where the locations with large plastic strains are circled. The U^*_M distribution and the associated main load paths of the bus bay section are elaborated in Figure 7.10b. As illustrated in Figure 7.10b, the load is mainly transferred to the window pillars instead of the roof pillars. Therefore, the large plastic strains mostly happened in the window pillars as can be seen in Figure 7.10b. The results also show that the major yielding points of the structure are all exactly located on the main load paths predicted by the U^*_M index. In order to upgrade the energy absorption, structural modifications are suggested to increase the contribution of the roof pillars in transferring the load.

On the other hand, it is difficult to obtain such load paths as shown in Figure 7.10b from the rollover simulation by LS-DYNA. Although the deformation result shown in Figure 7.10a indicates the roof pillars have smaller deformation than the window pillars, it is not sufficient to identify the reason behind this which could be either the roof pillars

have the higher stiffness or they are carrying less load. Hence, the load transfer analysis gives additional information with respect to the rollover simulation which are helpful for identifying the structural problems and improving the structural performance.

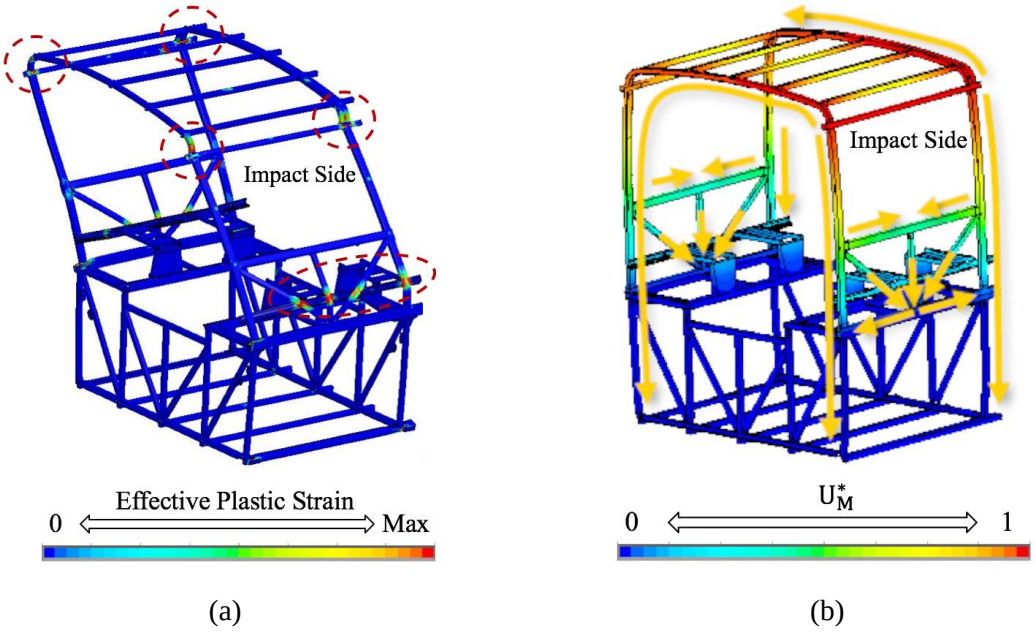

Figure 7.10: Computational results of the bus bay section- a): Maximum deformation during the rollover; b): U^*_M distribution and the main load paths (arrows).

In Figure 7.10a, the marked top corners of the bus bay section have severe plastic deformations. The U^*_M distribution of one of the corners is presented in Figure 7.11a while the U^*_M variation along the black arrow is shown in Figure 7.11b. It can be seen from Figure 7.11b that the decay of the U^*_M index in the curved section is remarkable faster than in the roof pillar. As a consequence, the stiffness of the curved section is far lower than the roof pillar with respect to the impact force. This is the reason that caused the severe plastic deformations to the top corners of the bus bay section.

In the desired situation, the energy absorption is uniform throughout the whole structure. This requires a uniform load transmission and stiffness distribution in the structure. Based on the result in Figure 7.11, the curved section needs to be enhanced in order to harmonize the stiffness distribution in the top corner of the bus bay section. The optimal design modification shall lead to a uniform decay speed of the U^*_M index in both roof pillar and curved section.

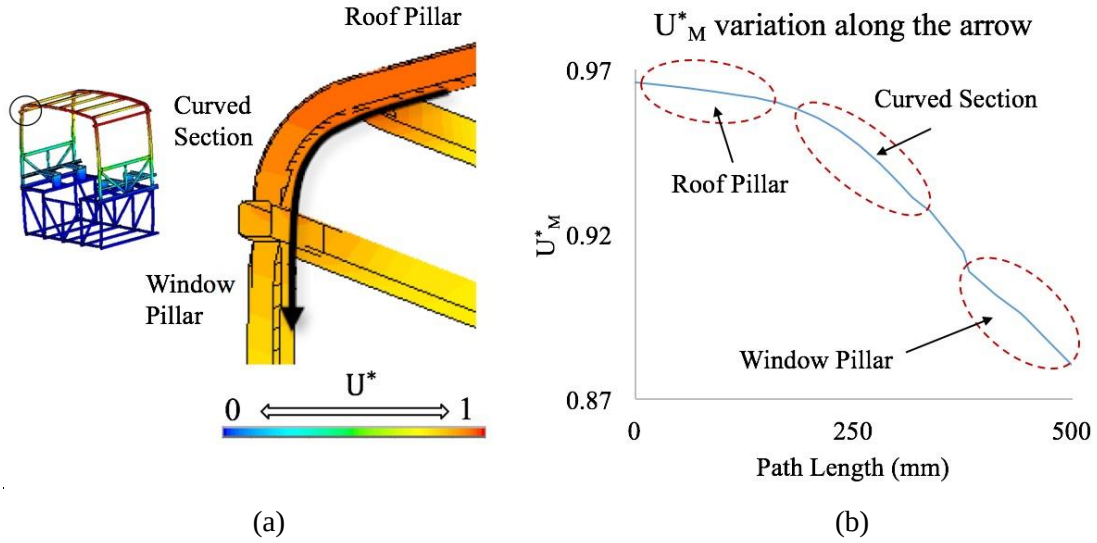

(a) (b)

Figure 7.11: Load transfer analysis of the top corner of the bus bay section- a): U^*_M distribution; b): U^*_M variations along the arrow.

Figure 7.12a shows U^*_M distribution and two paths at a cross point of the roof pillars. Figure 7.12b demonstrates the U^*_M variations of the two paths on the roof. As can be seen, the slope of the U^*_M curve of path-2 is significantly smaller than that of path-1. Hence, path-2 is the main load path rather than path-1. This result clearly reveals that the impact load is mainly transferred to the window pillars instead of the roof pillars. Hence, the roof did not effectively contribute to the energy absorption during the rollover collision. In order

to change the load path and make the roof pillars carry more impact load, extra pillars are suggested to be added between the loading point and the roof pillars.

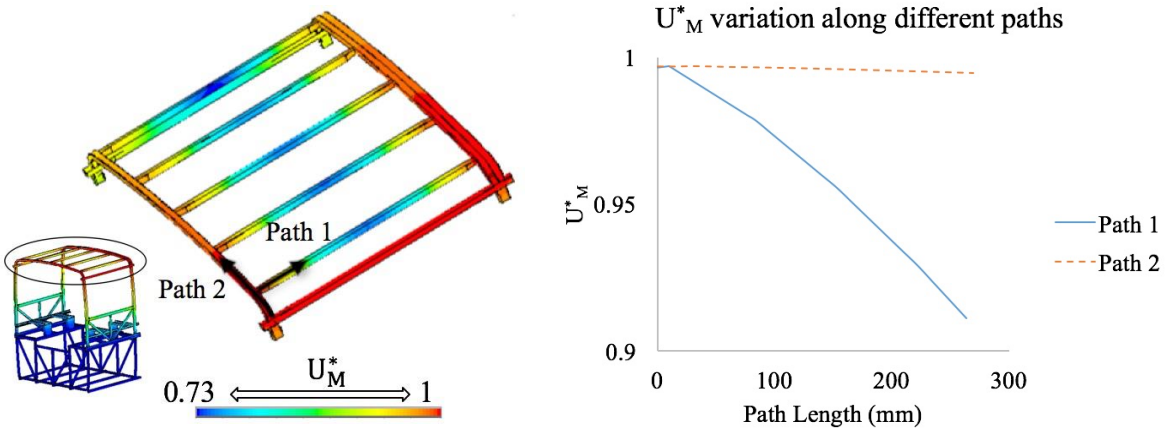

(a) (b)

Figure 7.12: U^*_M variations on the roof- a): U^*_M distribution and two paths; b): U^*_M variations along the paths.

Figure 7.13a presents three paths of the transferred force at a cross point on the window pillars of the bus bay section while Figure 7.13b shows the corresponding U^*_M values along those paths. The slope of path-3 is slightly lower than the other two, thus the force carried by path-3 is a little higher than path-4 and path-5. Nevertheless, considerable portion of the force is still transferred along path-4 and path-5. Although the difference of the transferred forces among these three pillars is small, harmonizing the load transfer among them can still improve the structural performance and efficiency.

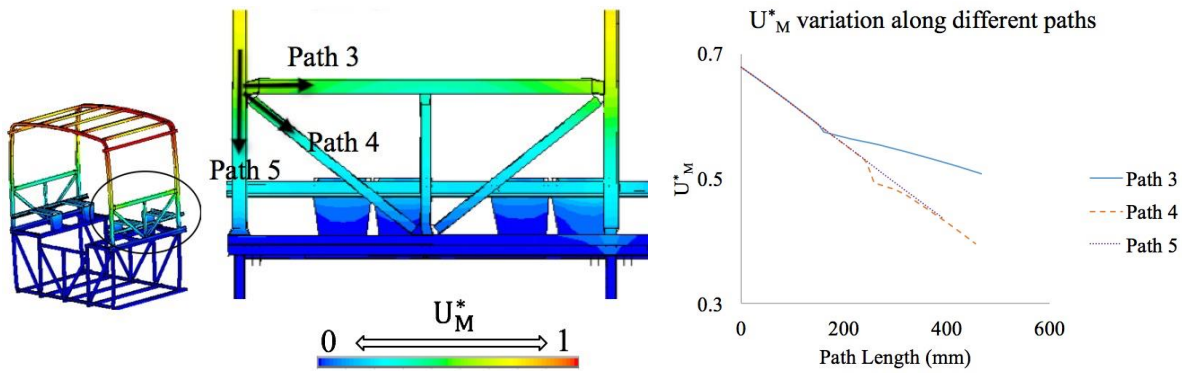

(a) (b)

Figure 7.13: U^*_M variations on the side wall- a): U^*_M distribution and three paths, b): U^*_M variations along the three paths.

7.4 Summary

Load transfer analysis is the foundation of load bearing structural design. This chapter introduced a means to compute the load paths of bus superstructures by considering the rollover impact. In this method, an equivalent static load was proposed to represent the impact force and the U^*_M index was used for calculating the load paths.

A bus bay section was used to demonstrate the proposed method while a rollover simulation of the bus bay section was performed using LS-DYNA as a reference to the load transfer analysis. The results indicate the presented load paths analysis based on the designed equivalent static load can reflect the major characteristics of the load transfer behavior of the bus bay section under the rollover impact. The proposed method can be generalized to study other kinds of bus collisions like frontal collisions.

Based on the proposed load transfer analysis, several structural issues were detected and the corresponding design recommendations were made for improving the performance of the energy absorption and the rationality of the stiffness distribution to the bus superstructure. It is hard to obtain the structural issues and the modification directions from the rollover simulation by LS-DYNA. Although the LS-DYNA simulation shows the failure locations, the reason of the failure is still inconclusive. The effective modification cannot be suggested by the rollover simulation due to the uncertainty in the reason of the failure.

The purpose of the study is to provide designers with supplementary information which can hardly be obtained from the conventional simulation approach. The conventional simulation approach such as the rollover simulation in this chapter has its own significance in structural analysis and it is irreplaceable based on the current study. The combination of the utilization of both methods can lead to more effective and efficient bus structural design than either of them.

Chapter 8

Conclusions and Perspectives

8.1 Contributions of the thesis

Load transfer analysis based on the U^* index has been used as a new design paradigm for vehicle structures. The original U^* index was constructed for isotropic materials and 3D continuum models (3 DOFs). In this thesis, the first experimental study of the U^* index theory was presented. The effectiveness of the U^* based design criteria was demonstrated. Two modified U^* indices have been successfully developed for load transfer analysis of vehicle structures. The proposed modified U^* indices (U^*_O and U^*_M) extended the application of the U^* index theory into orthotropic composite materials and mechanical models under six DOFs. Two applications were conducted based on real industrial problems to show the capability of the proposed U^*_M index. From the work of the thesis, following contributions have been realized.

***1) Experimental validation of the U^* index theory*:** The U^* index identifies the load path based on the internal stiffness between the loading point and any point in the structure. The route with the highest U^* values is the main load path. The thesis presented the first

experimental study on the U^* index theory. The tested load path form the experiment fully agrees with the calculated load path by the U^* index. It has been proved experimentally that the parts with higher U^* values indeed carry more load than other parts of the structure. The U^* is an accurate indicator of load paths in structures.

***2) The U^*_O index for orthotropic composite materials*:** The U^*_O index has been proposed as the more universal form than the original U^* index for load paths analysis of both orthotropic and isotropic materials. Two case studies show the U^*_O index predicts reasonable load paths for orthotropic composite structures. The weight-efficiency of the composite structures can be further increased based on load transfer analysis using the proposed U^*_O index.

***3) The U^*_M index for six DOFs systems*:** The load transfer index (U^*_M) under six DOFs mechanical systems has been successfully founded. The application of the full U^* index theory was expanded from 3D continuum models to six DOFs systems such as plate or shell models. It makes the U^* index theory more powerful and efficient for load transfer analysis of engineering structures especially thin-walled structures.

***4) Study of the implementation of the U^* based design criteria*:** The case studies introduced in Chapter 4 and Chapter 6 demonstrate that the U^* based design criteria are effective for improving the structural performance and weight-efficiency. The case studies can be used as a guide for applying the U^* based design criteria in vehicle structural design. In Chapter 6, the thickness reduction of the structure was achieved through the utilization of the U^*_M and U^*_{sum} indices, which is a novel application of the U^* index theory in structural design modification.

5) Load transfer analysis of bus structures for rollover protection: A means has been established to perform load transfer analysis of bus superstructures by considering rollover impact based on the U^*_M index. According to the legislated standard ECE R66, an equivalent static force was designed to represent the impact force during the rollover test. Thus, a complex nonlinear dynamic problem was simplified to be a linear static problem. The load transfer analysis can provide designers with additional information with respect to the conventional simulation method. The insights of the structural issues were investigated according to the load transfer analysis. Design recommendations were made for improving the bus structural performance during the rollover test.

8.2 Outlook of future work

The thesis focuses on the development of the U^* index theory. Based on the work of the thesis, several directions of the future study are recommended.

1. The thesis introduced the U^*_O index for extending the U^* index theory into composite materials. In future, applications of the U^*_O index in design analysis and optimization of complex composite structures are expected. Moreover, in the proposed validation testing, the experimental model is made by isotropic material. Hence, an experimental study of the U^*_O index on orthotropic composite materials is set as the future work of the thesis.

2. The U^* index theory has been mainly applied in automotive structures instead of aerospace structures. Nevertheless, load paths analysis is also a focus in aerospace engineering (Tamijani and Gharibi 2016). In future, applications of the U^* index theory to aerospace engineering are expected.

3. In Chapter 6 of the thesis, the mass to stiffness ratio of the sample structure was significantly improved by using the U^*_M and U^*_{sum} indices. The approach which leads to the thickness reduction showed great potential to be developed as a structural optimization method. This idea may be realized in the future study.

4. In Chapter 7, several design recommendations were made for improving the bus performance during rollover collision. The implementation of the corresponding design modifications to the bus structure is suggested as a future work.

5. Under violent collisions, vehicle structures would be subjected to plastic deformation. Currently, equivalent static loading method is widely used for load transfer analysis of vehicle collision, where the material is considered as linear elastic. However, to better investigate the load path variation during the vehicle collision, the extension of the U^* index theory into plastic deformation is needed.

Reference

Akima, S., Omiya, M., Takahashi, K.: Load Transfer of Passenger Car Compartment for Improvement of Structural Performance in Side Impact. In: 24th International Technical Conference on the Enhanced Safety of Vehicles (ESV). p. No. 15-0209 (2015).

ANSYS: ANSYS® Academic Research, Release 15.0,ANSYS Mechanical APDL Theory Reference, ANSYS, Inc. (2013).

ANSYS: ANSYS® Academic Research, Release 15.0, Help System, ANSYS, Inc., (2014).

Beer, F., Johnston, E., Dewolf, J., Mazurek, D.: Mechanics of Materials. 4th. McGraw Hill Higher Education (2006).

Casadei, A., Broda, R.: Impact of Vehicle Weight Reduction on Fuel Economy for Various Vehicle Architectures Impact of Vehicle Weight Reduction on Fuel Economy for Various Vehicle Architectures Prepared for: The Aluminum Association, Inc. (2008).

Chen, S.C., Chen, H.L., Hsu, P.M.: Effect of Molding Condition on Mechanical Properties of Injection Molded Nylon 6-Clay Nanocomposites. J. Reinf. Plast. Compos. 27, 1381–1395 (2008).

Christensen, P.W., Klarbring, A.: An Introduction to Structural Optimization. Springer

Netherlands, Dordrecht (2009).

Dornisch, W., Müller, R., Klinkel, S.: An efficient and robust rotational formulation for isogeometric Reissner–Mindlin shell elements. Comput. Methods Appl. Mech. Eng. 303, 1–34 (2016).

El-Abbasi, N., Meguid, S.A.: A Continuum Based Thick Shell Element for Large Deformation Analysis of Layered Composites. Int. J. Mech. Mater. Des. 2, 99–115 (2006).

Friedman, K., Hutchinson, J., Mihora, D., Kumar, S., Strickland, W.D.: Rollover protection for occupants of heavy truck sleeper cabs. Int. J. Crashworthiness. 20, 316–324 (2015).

Gharibi, K., Hurley, J., Tamijani, A.: Determination of Load paths in Plates and Shells Using Load Path Function. In: 58th AIAA/ASCE/AHS/ASC Structures, Structural Dynamics, and Materials Conference (2017).

Ghasemnejad, H., Hadavinia, H.: Off-axis Crashworthiness Characteristic of Woven Glass/Epoxy Composite Box Structures. J. Reinf. Plast. Compos. 29, 2306–2330 (2010).

Guler, M. a, Elitok, K., Bayram, B., Stelzmann, U.: The influence of seat structure and passenger weight on the rollover crashworthiness of an intercity coach∗. Int. J. Crashworthiness. 12, 567–580 (2007).

Harasaki, H., Arora, J.S.: New concepts of transferred and potential transferred forces in structures. Comput. Methods Appl. Mech. Eng. 191, 385–406 (2001)(a).

Harasaki, H., Arora, J.S.: A new class of evolutionary methods based on the concept of Transferred Force for structural design. Struct. Multidiscip. Optim. 22, 35–56 (2001)(b).

Reference

Harasaki, H., Arora, J.S.: Topology design based on transferred and potential transferred forces. Struct. Multidiscip. Optim. 23, 372–381 (2002).

Hoshino, H., Sakurai, T., Takahashi, K.: Vibration reduction in the cabins of heavy-duty trucks using the theory of load transfer paths. JSAE Rev. 24, 165–171 (2003).

Jones, R.: Mechanics of composite materials. CRC Press (1998).

Kelly, D., Reidsema, C., Bassandeh, A., Pearce, G., Lee, M.: On interpreting load paths and identifying a load bearing topology from finite element analysis. Finite Elem. Anal. Des. 47, 867–876 (2011).

Kelly, D.W., Hsu, P., Asudullah, M.: Load paths and load flow in finite element analysis. Eng. Comput. 18, 304–313 (2001).

Kobelev, V.: Exact shell solutions for conical springs. Mech. Based Des. Struct. Mach. 44, 317–339 (2016).

Koboyashi, H., Naito, T., Urushiyama., Y.: Study on Similarity of Load Path Distribution in Body Structure. Honda R&D Tech. Rev. 23.1. 80–89 (2011).

Li, C., Kim, I.Y., Jeswiet, J.: Conceptual and detailed design of an automotive engine cradle by using topology, shape, and size optimization. Struct. Multidiscip. Optim. 51, 547–564 (2015).

Li, R., Kelly, D., Crosky, A., Schoen, H., Smollich, L.: Improving the Efficiency of Fiber Steered Composite Joints using Load Path Trajectories. J. Compos. Mater. 40, 1645–1658 (2006).

Li, Y., Lan, F., Chen, J.: Experimental and Numerical Study of Rollover

Crashworthiness of a Coach Body Section. In: SAE Technical Paper: 2012-01-1900 (2012).

Liang, C.-C., Le, G.-N.: Bus rollover crashworthiness under European standard: an optimal analysis of superstructure strength using successive response surface method. Int. J. Crashworthiness. 14, 623–639 (2009).

Liang, C.-C., Le, G.-N.: Analysis of bus rollover protection under legislated standards using LS-DYNA software simulation techniques. Int. J. Automot. Technol. 11, 495–506 (2010).

LSTC: LS-DYNA Keyword User's Manual. Livermore Software Technology Corporation (LSTC) (2015).

Marhadi, K., Venkataraman, S.: Comparison of Quantitative and Qualitative Information Provided by Different Structural Load Path Definitions. Int. J. Simul. Multidiscip. Des. Optim. 3, 384–400 (2009).

MTS: MTS System Corporation, https://www.mts.com/en/products/application/materials-testing/index.htm.

Naito, T., Kobayashi, H., Urushiyama, Y.: Application of Load Path Index U* for Evaluation of Sheet Steel Joint with Spot Welds. In: SAE Technical Paper 2012-01-0534 (2012).

Naito, T., Kobayashi, H., Urushiyama, Y., Takahashi, K.: Introduction of New Concept U*sum for Evaluation of Weight-Efficient Structure. SAE Int. J. Passeng. Cars - Electron. Electr. Syst. 4, 30–41 (2011).

Reference

Niordson, F.I.: Shell theory. Elsevier (2012).

Palmisano, F., Elia, A.: Assessment of masonry buildings subjected to landslide by using the load path method. Int. J. Civ. Eng. 12, 312–330 (2014).

Park, S.J., Yoo, W.S., Kwon, Y.J.: Rollover analysis of a bus using beam and nonlinear spring elements. WSEAS Trans. Math. 5, 526–531 (2006).

Pegoretti, A., Fambri, L., Zappini, G., Bianchetti, M.: Finite element analysis of a glass fibre reinforced composite endodontic post. Biomaterials. 23, 2667–2682 (2002).

Pejhan, K., Kuznetcov, A., Wang, Q., Wu, C.Q., Telichev, I.: Design assessment of a multiple passenger vehicle component using load transfer index (U*) method. Int. J. Mech. Mater. Des. 1–17 (2017)(a).

Pejhan, K., Wang, Q., Telichev, I.: Experimental Study of U* Index Response to Structural and Loading Variations. In: ASME 2015 International Mechanical Engineering Congress and Exposition. p. V009T12A010 (2015)(a).

Pejhan, K., Wang, Q., Wu, C.Q., Telichev, I.: Extension of U* Index Theory to Nonlinear Case of Load Transfer Analysis. In: ASME 2015 International Mechanical Engineering Congress and Exposition. p. V009T12A008 (2015)(b).

Pejhan, K., Wang, Q., Wu, C.Q., Telichev, I.: Experimental Validation of the U* index Theory for Load Transfer Analysis. Int. J. Heavy Veh. Syst. 24, 288–304 (2017)(b).

Pejhan, K., Wu, C.Q., Telichev, I.: Comparison of load transfer index (U*) with conventional stress analysis in vehicle structure design evaluation. Int. J. Veh. Des. 68, 285–303 (2015)(c).

Reference

Roca, T., Arbiol, J., Ruiz, S.: Development of Rollover-Resistant Bus Structures. In: SAE Technical Paper: 970581 (1997).

Sakurai, T., Tada, M., Ishii, H.: Load path U* analysis of structures under multiple loading conditions. Japan Soc. Mech. Eng. 73, 15–20 (2007)(a).

Sakurai, T., Takahashi, K., Kawakami, H., Abe, M.: Reduction of Calculation Time for Load Path U* Analysis of Structures. J. Solid Mech. Mater. Eng. 1, 1322–1330 (2007)(b).

Sakurai, T., Tanaka, J., Otani, A., Zhang, C., Takahashi, K.: Load Path Optimization and U * Structural Analysis for Passenger Car Compartments under Frontal Collision. In: SAE Technical Paper 2003-01-2734 (2003).

Scientists, U. of C.: Car Emissions and Global Warming, http://www.ucsusa.org/clean_vehicles/why-clean-cars/global-warming/.

Serra, M.: Design of Membrane Shells of Revolution with Optimal Stiffness. Mech. Based Des. Struct. Mach. 38, 403–416 (2010).

Simkins, D.C., Li, S.: Effective bending stiffness for plates with microcracks. Arch. Appl. Mech. 73, 282–309 (2003).

Simo, J.C., Armero, F.: Geometrically non-linear enhanced strain mixed methods and the method of incompatible modes. Int. J. Numer. Methods Eng. 33, 1413–1449 (1992).

Takahashi, K.: Relative Rigidity of structures and Saint Venant's Principle. Trans. Japan Soc. Mech. Eng. Ser. A. 52, 2615–2621 (1986).

Takahashi, K., Omiya, M., Iso, T., Zaiki, Y., Sakurai, T., Maki, T., Urushiyama, Y., Naito, T.: Load transfer ustar (U*) calculation in structures under dynamic loading. Trans.

Japan Soc. Mech. Eng. Part A. 79, 1657–1668 (2013).

Takahashi, K., Sakurai, T.: Expression of Load Transfer Paths in Structures. Trans. Japan Soc. Mech. Eng. Ser. A. 71, 1097–1102 (2005).

Tamijani, A., Gharibi, K.: Load Paths Visualization in Plane Elasticity Using Load Path Function Method. In: 57th AIAA/ASCE/AHS/ASC structures, structural dynamics, and materials conference. , San Diego (2016).

Tarlochan, F., Ramesh, S.: Composite sandwich structures with nested inserts for energy absorption application. Compos. Struct. 94, 904–916 (2012).

UNECE: Strength of the superstructure of large passenger vehicles, Regulation No. 66, http://www.unece.org/trans/main/wp29/wp29regs61-80.html.

VISTA: Vista Medical-Pressure Mapping, Pressure Sensing and Pressure Imaging products, http://www.pressuremapping.com/index.cfm?pageID=13&section=37.

Wang, E., Yoshikuni, Y., Guo, Q., Nohara, T., Ishii, H., Hoshino, H., Takahashi, K.: Load Transfer in Truck Cab Structures under Initial Phase of Frontal Collision. Int. J. Veh. Struct. Syst. 2, 60–68 (2010).

Wang, Q., Pejhan, K., Telichev, I., Wu, C.Q.: Extensions of the U* Theory for Applications on Orthotropic Composites and Nonlinear Elastic Materials. Int. J. Mech. Mater. Des. 13, 469–480 (2017)(a).

Wang, Q., Pejhan, K., Telichev, I., Wu, C.Q.: Demonstration of the Effectiveness of U* Based Design Criteria on Vehicle Structural Design. Proc. Inst. Mech. Eng. Part D J. Automob. Eng. 1–8 (2017)(b).

Reference

Wang, Q., Pejhan, K., Wu, C.Q., Telichev, I.: Load Transfer Index for Composite Materials. In: ASME 2015 International Mechanical Engineering Congress and Exposition. p. V009T12A009 (2015).

Wang, Q., Telichev, I., Wu, C.Q.: A New Load Transfer Index (U*M) with Considering Six Degrees of Freedom and Its Application in Structural Design and Analysis. Mech. Based Des. Struct. Mach. A Int. J. 1–15 (2017)(c).

Zhang, J., Chaisombat, K., He, S., Wang, C.H.: Hybrid composite laminates reinforced with glass/carbon woven fabrics for lightweight load bearing structures. Mater. Des. 36, 75–80 (2012).

Zhang, Y.X., Yang, C.H.: Recent developments in finite element analysis for laminated composite plates. Compos. Struct. 88, 147–157 (2009).

Appendix: User-defined ANSYS Code for U^* Calculation

In the thesis, the mathematical formulation of the U^* index was presented in Chapter 2.1. Then, the load paths were obtained by manually connecting the highest U^* values. In Chapter 2.4, a flowchart for U^* algorithm programming was provided. To help readers to develop their own codes to calculate U^* index, an example of user-defined ANSYS code for U^* computation is given below.

```
!!!!!!!!!!!!!!!!!!!!! User-defined ANSYS code for U* computation!!!!!!!!!!!!!!!!!!!!!!!!!!!!

Finish

!!!!!!!!!!Define an array to store U* values!!!!!!!!!!!!!!!!!!!

/nerr,,9999999

/PREP7

*get,nodenum,node,,num,max

*dim,Ustar,,nodenum

fdele,all,all

ddele,all,all

!!!!!!!!!!!!!!!Define boundary conditions!!!!!!!!!!!!!!!!!!!

D,BC,all,0

D,2790,all,0

D,2790,UX,0.01367

!!!!!!!!!!!!! Calculation of total strain energy of original system!!!!!!!!!!!
```

```
/SOL
ANTYPE,0
NSUBST,1,0,0
OUTRES,ALL,ALL
TIME,1
/STATUS,SOLU
SOLVE
/POST1
 ETABLE,SEN,SENE
 SSUM
*get,U0,SSUM,0,item1,sen
finish
!!!!!!!! Calculation of total strain energy of modified (point C is fixed) system!!!!!!!
*do,i,1,nodenum
/PREP7
fdele,all,all
ddele,all,all
D,i,ALL,          0.0
D,BC,all,0
D,2790,all,0
D,2790,UX,0.01367
/SOL
ANTYPE,0
NSUBST,1,0,0
OUTRES,ALL,ALL
TIME,1
/STATUS,SOLU
```

```
SOLVE
/POST1
 ETABLE,SEN,SENE
 SSUM
!!!!!!!!!!!!Calculate U* and store the values into the early defined array!!!!!!!!!
*get,Un,SSUM,0,item1,sen
Ustar(i)=1-U0/Un
!!!!!!!!!!!!Assign U* values to each node as temperature (body force)!!!!!!!!!
/PREP7
bf,i,temp,Ustar(i)
/SOL
/STATUS,SOLU
SOLVE
/POST1
*enddo
!!!!!!!Write U* values into a user-defined text file!!!!!!!!!!!!!!!!
*cfopen,Ustar_R_G,txt
*vwrite,Ustar(1)
(F10.6)
*cfclos
finish
```